锦屏太阳和地球中微子实验中的放射性核衰变研究

（申请清华大学工学博士学位论文）

培 养 单 位 ： 工 程 物 理 系

学　　　科 ： 核 科 学 与 技 术

研 究 生 ： 古 兰 姆

指 导 教 师 ： 陈 少 敏 教 授

副 指 导 教 师 ： 王 喆 副 教 授

二〇一七年五月

Radioactive Nucleus Decays for Solar and Geoneutrino Experiment at Jinping

Dissertation Submitted to

Tsinghua University

in partial fulfillment of the requirement

for the degree of

Doctor of Philosophy

in

Nuclear Science and Technology

by

Ghulam Hussain

Dissertation Supervisor : Professor CHEN Shaomin
Associate Supervisor : Professor WANG Zhe

May, 2017

关于学位论文使用授权的说明

本人完全了解清华大学有关保留、使用学位论文的规定，即：

清华大学拥有在著作权法规定范围内学位论文的使用权，其中包括：（1）已获学位的研究生必须按学校规定提交学位论文，学校可以采用影印、缩印或其他复制手段保存研究生上交的学位论文；（2）为教学和科研目的，学校可以将公开的学位论文作为资料在图书馆、资料室等场所供校内师生阅读，或在校园网上供校内师生浏览部分内容；（3）根据《中华人民共和国学位条例暂行实施办法》，向国家图书馆报送可以公开的学位论文。

本人保证遵守上述规定。

（保密的论文在解密后应遵守此规定）

作者签名：_____　　　导师签名：_____

日　　期：_____　　　日　　期：_____

摘　要

　　中微子目前已经成为粒子物理、核物理、天体物理与宇宙学研究中共同关注的一个热点课题，具有重要的科学意义与应用价值。在世界上最深的中国锦屏地下实验室（CJPL）开展低能中微子实验，具有最低的宇宙线本底与反应堆中微子本底，以及理论预期有最高的地球中微子流强的天然优势，特别适合于开展对太阳中微子和地球中微子的相关物理研究。本论文针对锦屏太阳与地球中微子实验密切相关的放射性核衰变问题及应用进行了研究，主要创新点如下

　　1) 对用于建造锦屏中微子探测器的不锈钢原材料、加工工艺与市场上供应的商品和专门定制的样品进行了比较分析。利用锦屏地下实验室低本底环境下的高纯锗探测器，对样品的放射性同位素铀、钍、钾，甚至包括微量的钴和铯进行了测量，精度达到了每千克毫贝克的水平。研究结果表明，定制的不锈钢样品本底水平达到了实验的要求。

　　2) 分析了产生地球中微子的天然放射性同位素铀-238、钍-232和钾-40衰变链及其贝塔衰变的中微子能谱。并且还对影响地球中微子测量的反应堆中微子本底进行了研究。最后还结合中微子振荡理论，给出了在锦屏的地球中微子信号通量以及反应堆中微子本底通量的估计。

关键词：中微子; 地球中微子; 太阳中微子; 放射性; 锦屏

Abstract

Neutrinos have been a common interest among the study of particle physics, nuclear physics, astrophysics and cosmology, and hence have important scientific significance and great potential application. The proposed low-energy neutrino experiment at China JinPing underground Lab (CJPL) with the largest overburden in the world, has natural advantages of lowest cosmic background and reactor neutrino background, as well as the highest geoneutrino flux, specifically suitable for relevant physics studies on solar neutrinos and geoneutrinos. This thesis focuses on the issues and applications of the radioactive nucleus decays for the solar and geoneutrino experiment at Jinping. The studies are as follows:

1) We analyzed the samples for the stainless steel to be used in building a neutrino detector at Jinping, including the raw iron, the smelting process, the commercial and custom-made products. Exploiting the low background facility at Jinping, we used the High Purity Germanium detector (HPGe) to measure the radioactivity of U, Th and K, even for the tiny Co and Cs contaminations. The accuracy reaches to the level of mBq/kg. Our study indicates that the custom-made stainless steel samples meet the requirement at Jinping.

2) We investigated natural radioactive isotopes ^{238}U, ^{232}Th and ^{40}K decay chains, together with the neutrino spectra from their beta decays. We also studied the reactor neutrino background, which is major background of geoneutrino experiments. In the end, we applied the neutrino oscillation theory to the evaluation of the geoneutrino signal and the reactor neutrino background fluxes.

Key words: neutrino; geo-neutrino; solar neutrino; radioactivity; Jinping

Contents

List of main acronyms

SM	Standard Model
MC	Monte Carlo
E	Energy
M	Mass
p	Momentum
t	Time
ϵ	Efficiency
BF	Branching fraction
TeV/GeV/MeV/keV	Tera/Giga/Mega/Kilo electron volt
TW	Terawatt
TNU	Terrestrial neutrino units
IBD	Inverse beta decay
Bq	Bcqueral
Km	Kilometer
U	Uranium
Th	Thorium
K	Potassium
Pb	Lead
Cu	Copper
ppb	Part per billion
ppm	Part per million
NPP	Nuclear power plant
AD	Antineutrino detector
SST	Stainless steel
IBD	Inverse beta decay
PMT	Photomultiplier tubes
p.e.	Photoelectron
LAB	Linear alkyl benzene
CJPL	China Jinping underground laboratory
GDMS	Glow discharge mass spectrometer
HPGe	High purity germanium

FWHM   Full width half maximum

THU   Tsinghua University

Chapter 1   Introduction

In 1930, Pauli proposed a weakly interacting neutral particle[1]. He tried to explain the continuum energy distribution in the beta decay process. The proposed particle (neutrino) was later experimentally verified by Reines and Cowan in 1956, at the Savannah River Experiment. They are the pioneers to give birth of electron antineutrino ($\bar{\nu}_e$) experimentally[2]. Later on two more flavours of neutrino (ν_μ and ν_τ) were discovered by[3,4]. All flavours of neutrinos are the fundamental ingredients of the Standard Model, only interacting through the weekly interactions. Pontecorvo was a pioneer to give the idea of neutrino oscillations[5], which were confirmed by experiments. Today, because of it's unique features, the study of neutrino has been a common interest among particle physics, nuclear physics, astrophysics, cosmology and geo-science.

1.1   Standard Model neutrinos

Neutrinos are fundamental particles of the Standard Model and appear in three flavor generations which only couple to another lepton as shown in Fig. 1.1. The electron neutrino (ν_e), the tau neutrino (ν_τ) and the muon neutrino (ν_μ), are three flavors of the neutrinos, each type relating to its charge partner: the electron (e^-), the tau (τ^-) and the muon (μ^-) respectively, as shown in Matrix (1-1). A pair of these three particles and their antiparticles makes up individual groups of elementary particles recognized as leptons.

$$\begin{pmatrix} \nu_e \\ e^- \end{pmatrix}, \quad \begin{pmatrix} \nu_\mu \\ \mu^- \end{pmatrix}, \quad \begin{pmatrix} \nu_\tau \\ \tau^- \end{pmatrix}. \tag{1-1}$$

Leptons are spin 1/2 fermions and can only interact through weak force, electromagnetic force and gravitational force. Neutrinos are different from the charged leptons because they are charge-less (having no electric charge) and with negligible mass. From weak interactions, which produce neutrinos, a fundamental symmetry is born in the conservation of lepton number. When one lepton is produced in the interaction, an anti-lepton should also be produced to conserve the number of leptons universally. This can be explained by the production of an (ν_e) and ($\bar{\nu}_e$) neutrino in β decay.
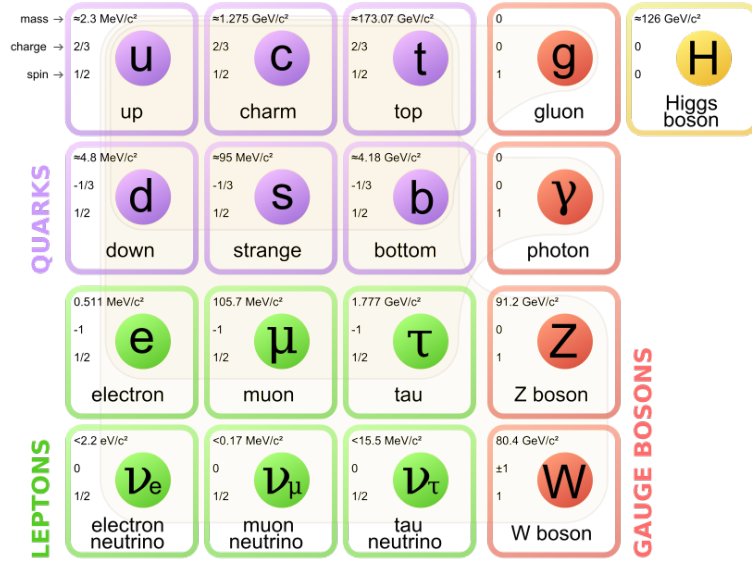
Figure 1.1   Fundamental particles in Standard Model [6].

1.1.1 Neutrino survival probability

Neutrino oscillation probability can be represented as neutrino flavor eigenstates, which are linear combination of the mass eigenstates [6].

$$|\nu_\alpha\rangle = \sum_k U_{\alpha k}^*|\nu_k\rangle, \tag{1-2}$$

where α indicates the neutrino flavors e, μ, τ; k indicates the mass eigenstates states; U is the mixing matrix. The mass eigenstates $|\nu_k\rangle$ are the eigenstates of the Hamiltonian with the eigenvalues Eq. (1-3)

$$E_k = \sqrt{\vec{p}^2 + m_k^2}, \tag{1-3}$$

$$\mathcal{H}|\nu_k\rangle = E_k|\nu_k\rangle. \tag{1-4}$$

From Schrödinger's equation,

$$i\frac{d}{dt}|\nu_k(t)\rangle = \mathcal{H}|\nu_k(t)\rangle, \tag{1-5}$$

we obtain the time evolution of massive neutrino eigenstates,

$$|\nu_k(t)\rangle = e^{-iE_kt}|\nu_k\rangle. \tag{1-6}$$

From, Eqs. (1-2) and (1-6), we have,

$$|\nu_\alpha(t)\rangle = \sum_k U_{\alpha k}^* e^{-iE_kt}|\nu_k\rangle. \tag{1-7}$$

By the unitary relation, Eq. (1-2) can be rewritten as

$$|\nu_k\rangle = \sum U_{\alpha k}|\nu_\alpha\rangle. \tag{1-8}$$

The time evolution of flavor state α is

$$|\nu_\alpha(t)\rangle = \sum_\beta \left(\sum_k U_{\alpha k}^* e^{-iE_kt} U_{\beta_k} \right)|\nu_\alpha\rangle. \tag{1-9}$$

The transition amplitude for $\nu_\alpha \to \nu_\beta$ is given by

$$A_{\nu_\alpha \to \nu_\beta} \equiv \langle \nu_\beta | \nu_\alpha \rangle = \sum_k U_{\alpha k}^* U_{\beta k} e^{-iE_kt}. \tag{1-10}$$

Therefore, the probability for ν_α oscillating into ν_β is

$$P_{\nu_\alpha \to \nu_\beta}(t) \equiv |A_{\nu_\alpha \to \nu_\beta}(t)|^2 = \sum_k U_{\alpha k}^* U_{\beta k} U_{\alpha j} U_{\beta j}^* e^{-i(E_k-E_j)t}. \tag{1-11}$$

For uncharacteristic neutrinos, ν's propagate at the speed of light, so we can ignore the neutrino mass and have the energy with $E = |\vec{p}|$ and $E_k \simeq E + \frac{m_k^2}{2E}$. We then obtain

$$P_{\nu_\alpha \to \nu_\beta}(t) = \sum_{kj} U_{\alpha k} U*_{\beta k} U_{\alpha j}^* U_{\beta j}.exp\left(-i\frac{\Delta m_{kj}^2 t}{2E} \right). \tag{1-12}$$

Using the unitary relation,

$$\sum_k |U_{\alpha k}|^2 |U_{\beta k}|^2 = \delta_{\alpha\beta} - 2\sum_{kj} \Re[U_{\alpha k}^* U_{\beta k} U_{\alpha j} U_{\beta j}^*], \tag{1-13}$$

we rewrite Eq. (1-2) into[7]

$$
\begin{aligned}
P_{\nu_\alpha \to \nu_\beta}(L, E) =& \delta_{\alpha\beta} - 4 \sum_{k>j} \Re[U_{\alpha k}^* U_{\beta k} U_{\alpha j} U_{\beta j}^*] \sin^2\left(\frac{\Delta m_{kj}^2 L}{4E}\right) \\
& + 2 \sum_{k>j} I[U_{\alpha k}^* U_{\beta k} U_{\alpha j} U_{\beta j}^*] \sin\left(\frac{\Delta m_{kj}^2 L}{2E}\right),
\end{aligned}
\tag{1-14}
$$

For the antineutrino case, $\bar{\nu}_\alpha$, one has

$$
|\bar{\nu}_\alpha\rangle = \sum_k U_{\alpha k} |\bar{\nu}_k\rangle.
\tag{1-15}
$$

Hence the probability for the oscillation $\bar{\nu}_\alpha \to \bar{\nu}_\beta$ is

$$
\begin{aligned}
P_{\bar{\nu}_\alpha \to \bar{\nu}_\beta}(L, E) =& \delta_{\alpha\beta} - 4 \sum_{k>j} \Re[U_{\alpha k}^* U_{\beta k} U_{\alpha j} U_{\beta j}^*] \sin^2\left(\frac{\Delta m_{kj}^2 L}{4E}\right) \\
& - 2 \sum_{k>j} I[U_{\alpha k}^* U_{\beta k} U_{\alpha j} U_{\beta j}^*] \sin\left(\frac{\Delta m_{kj}^2 L}{2E}\right).
\end{aligned}
\tag{1-16}
$$

The above probability is called as the survival probability for $\alpha = \beta$, while it becomes a transition probability for $\alpha \neq \beta$. For three neutrino flavors, the matrix expression of Eq. (1-2) is

$$
\begin{bmatrix} \nu_e \\ \nu_\mu \\ \nu_\tau \end{bmatrix} = U_{PMNS} \begin{bmatrix} \nu_1 \\ \nu_2 \\ \nu_3 \end{bmatrix},
$$

where U_{PMNS} is the mixing matrix is known as Pontecorvo-Maki-Nakagawa-Sakata matrix,

$$
U_{PMNS} = \begin{pmatrix} U_{e1} & U_{e2} & U_{e3} \\ U_{\mu 1} & U_{\mu 2} & U_{\mu 3} \\ U_{\tau 1} & U_{\tau 2} & U_{\tau 3} \end{pmatrix}
$$

$$
\begin{pmatrix} 1 & 0 & 0 \\ 0 & C_{23} & S_{23} \\ 0 & -S_{23} & C_{23} \end{pmatrix} \begin{pmatrix} C_{13} & 0 & S_{13}e^{-i\delta_{CP}} \\ 0 & 1 & 0 \\ C_{13}e^{-i\delta_{CP}} & 0 & S_{13} \end{pmatrix} \begin{pmatrix} C_{12} & S_{12} & 0 \\ -S_{12} & C_{12} & 0 \\ 0 & 0 & 1 \end{pmatrix}
\tag{1-17}
$$

$$
\begin{pmatrix} C_{12}C_{13} & C_{13}S_{12} & S_{13}e^{-i\delta} \\ -C_{23}S_{12} - S_{13}C_{12}S_{23}e^{i\delta} & C_{23}S_{12} - S_{13}S_{12}S_{23}e^{i\delta} & C_{13}S_{23} \\ S_{23}S_{12} - S_{13}C_{12}C_{23}e^{i\delta} & -S_{23}C_{12} - & S_{13}S_{12}S_{23}e^{i\delta} \quad C_{13}C_{23} \end{pmatrix}
\tag{1-18}
$$

where $C_{jk} = \cos\theta_{jk}$, $S_{jk} = \sin\theta_{jk}$.

In Eq. (1-18), there are six parameters to describe the mixing matrix of the three-flavor neutrino oscillations. The six parameters are the three mixing angle, θ_{jk}, two mass squared difference $\Delta m_{jk}^2 = m_j^2 - m_k^2$, and one CP-violation phase, δ_{CP}. From the current experiments, $\sin^2\theta_{23}$ and $\sin^2\theta_{12}$ are $0.386^{+0.024}_{-0.021}$ and $0.307^{+0.018}_{-0.016}$ [6], while Δm_{21}^2 is $7.50^{+0.19}_{-0.20} \times 10^{-5}$ eV^2 and Δm_{31}^2 is $(2.4 \pm 0.1) \times 10^{-3}$ eV^2.

For reactor neutrino experiments, we take $\alpha = e$ and $\beta = e$ such that

$$P_{\bar{\nu}_\alpha \to \bar{\nu}_\beta}(L, E) = 1 - 4 \sum_{k>j} \Re[U_{\alpha k}^* U_{\beta k} U_{\alpha j} U_{\beta j}^*] \sin^2(\frac{\Delta m_{kj}^2 L}{4E}), \tag{1-19}$$

the survival probability becomes

$$P_{\bar{\nu}_e \to \bar{\nu}_e}(L, E) = 1 - \sin^2 2\theta_{13}\left[\sin^2_{\theta_{12}} \sin^2(\frac{\Delta m_{32}^2 L}{4E}) + \cos^2\theta_{12} \sin^2(\frac{\Delta m_{31}^2 L}{4E})\right]$$
$$- \cos^4_{\theta_{13}} \sin^2 2\theta_{12} \sin^2 \frac{\Delta m_{21}^2 L}{4E}, \tag{1-20}$$

For the realistic unit, $\frac{\Delta m_{kj}^2 L}{4E}$ is rewritten as $\frac{\Delta m_{kj}^2 c^4 \cdot L}{4\hbar c E}$ where $\hbar c = 197.33 \times$ eV.m, such that

$$\frac{\Delta m_{kj}^2 c^4}{4\hbar c} \cdot \frac{L}{E} = \frac{\Delta m_{kj}^2 c^4}{4 \cdot 197 \times 10^{-9}} \cdot \frac{L}{E} \sim 1.267 \cdot \frac{\Delta m_{kj}^2 (eV^2) L(km)}{E(GeV)}. \tag{1-21}$$

If we take the inputs $E = 3.5$ MeV, $\Delta m_{31}^2 \sim \Delta m_{32}^2 = 2.232 \times 10^{-3}$ eV^2, $\Delta m_{21}^2 = 7.59 \times 10^{-5}$ eV^2 and $\sin^2 2\theta_{12} = 0.861$ [6]. The survival probability vs. the baseline L is shown in Fig. 1.2.
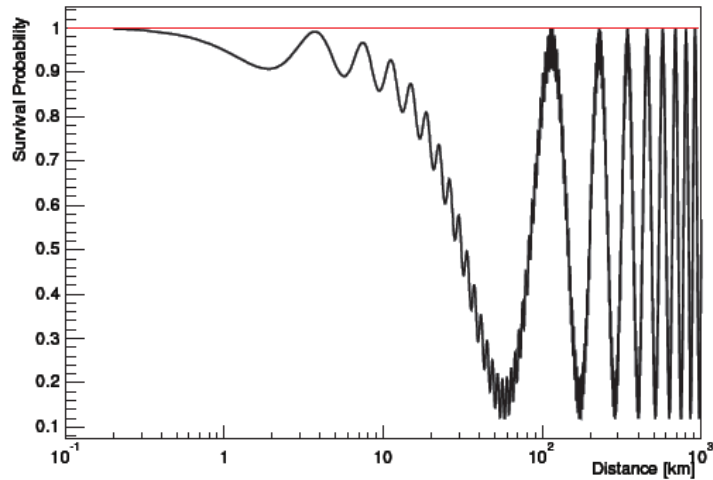
Figure 1.2   Survival probability vs. baseline [8].

1.1.2   Neutrino sources

Figure 1.3 shows different flavours of neutrinos that reach to the Earth's surface. The spectra can further be extended in terms of intensity and energy, excluding the reactors and accelerators neutrino flux, where the flux depends upon the position of the detector. In this thesis, reactor neutrinos, geoneutrinos and solar neutrinos will be discussed briefly.
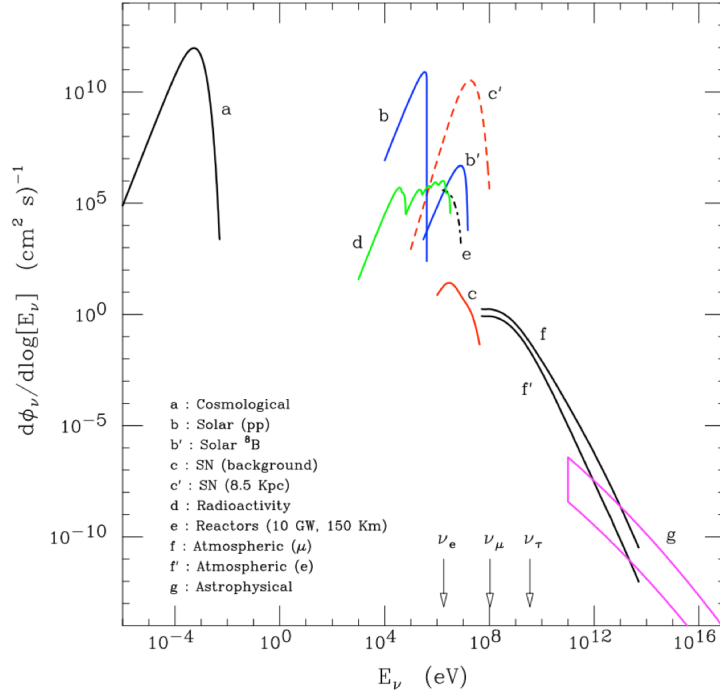
Figure 1.3   Neutrino fluxes for all the flavours in the world. The arrows indicate the three flavour's threshold for charge current (CC) interaction with free proton target. Those from the radioactive decay chains of ^{232}Th and ^{238}U are also shown[9].

- Reactor neutrinos are the major man-made source of neutrinos from the β decay of the products of nuclear reactors. Fissions of ^{235}U, ^{238}U, ^{239}Pu and ^{241}Pu provides the major source of energy in the nuclear reactor. The reactor anti-neutrino spectrum has been studied by several experiments, e.g. DayaBay[10] and RENO[11].
- Geoneutrinos are electron anti-neutrinos ($\bar{\nu}_e$'s) from the terrestrial region. These neutrinos are produced by beta decays within the Earth. By calculating the geo-neutrinos flux arriving from the terrestrial origin, it is possible to know the number of beta decay reactions taking place, and from this we can also extrapolate the heat being produced by the decay series. In the same way, by knowing the flux at various places around the world, one can plot the map of heat distribution and

determine the uniformity of radioisotope.

- Solar ν's are formed through nuclear fusion processes within the Sun. Each nuclear fusion reaction has a different Q-value, which is determined by the mass difference between the reactants and products. There are various nuclear reactions which happen inside the sun, the dominant source of neutrinos is from proton-proton (pp) fusion[12]. The solar ν flux as a function of energy can be seen in the Fig. 5.10.

$$4p \rightarrow^4 He + 2e^+ + 2\nu_e + Q = 26.7 \text{ MeV}. \tag{1-22}$$
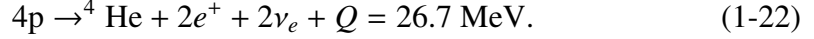
- Atmospheric neutrinos are formed from cosmic rays interacting with atoms in the upper atmosphere. The resultant products are hadrons which are composed mostly of pions[13]. The pion decay channels, which produce neutrinos, are shown in Eq. (1-23):

$$\pi^\pm \rightarrow \mu^\pm + \nu_\mu(\bar{\nu}_\mu),$$
$$\searrow \tag{1-23}$$
$$e^\pm + \nu_e(\bar{\nu}_e) + \bar{\nu}_\mu(\nu_\mu).$$
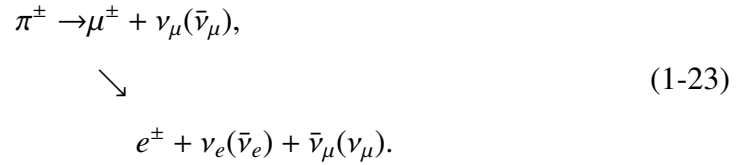
- Cosmological neutrinos are the residuals from the Big Bang explosions (since early universe) and similar to cosmic microwave background photons. Three flavours and anti-flavours of neutrinos have a density of ~ 56 cm^{-3} with a black body visible spectrum at low temperature $T_\nu = 1.9$ K. The flux of cosmological neutrinos relies on the mass of specific neutrino species. The flux has been estimated to be $\sim 4 \times 10^{10}$ cm^{-2}s^{-1} for each ν flavour with the upper limit of $m_\nu < 2$ eV[14].

1.2   Solar neutrinos

In 1939, Bethe[15] explained that the Sun glows due to the interior nuclear fusion process Eq. (1-24):

$$4p \rightarrow^4 He + 2e^+ + 2\nu_e + Q = 26.7 \text{ MeV}. \tag{1-24}$$
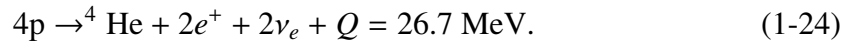
The general fusion Eq. (1-24) can go through with several reaction chains that produce the same end-products, with different energy spectra of ν's. The major fusion cycles are shown in Fig. 1.4. This light-element fusion cycles account for about 98.5% of the energy in the Sun's interior, while the rest are from from heavy-element fusion cycle, which is

carbon-nitrogen-oxygen (CNO) cycle in the Sun and the major one occurring in heavy high temperature stars. The neutrino fluxes of different cycles are shown in Fig. 5.10.
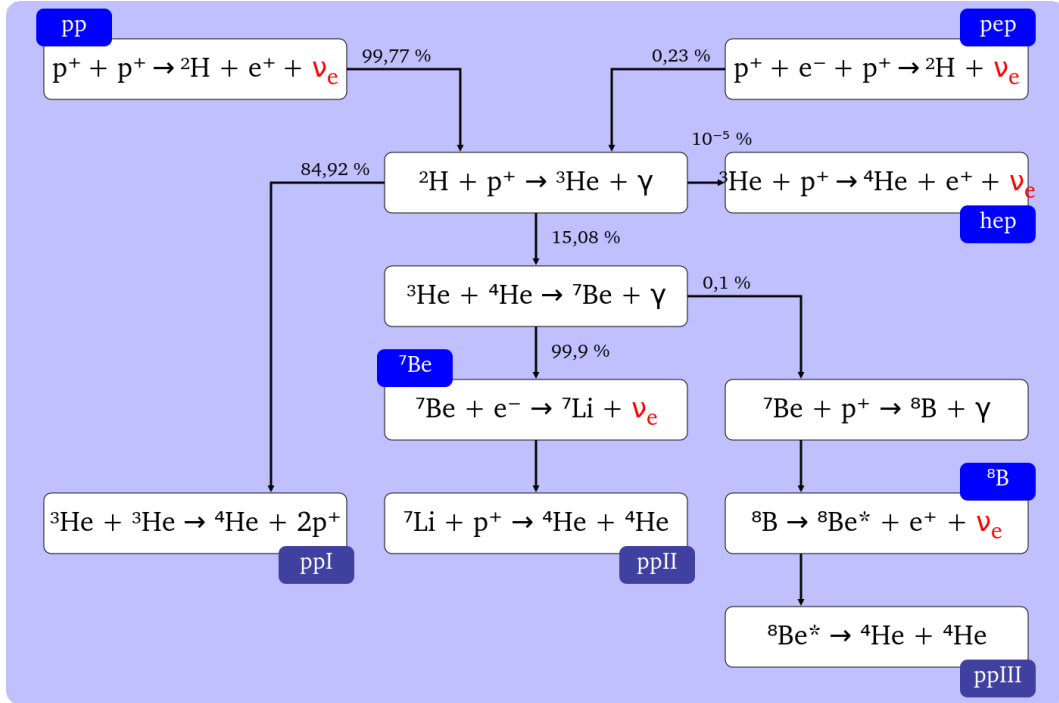
Figure 1.4   The production of neutrinos by *pp* the chain and others in the interior of the Sun (Figure taken from Wikipedia).
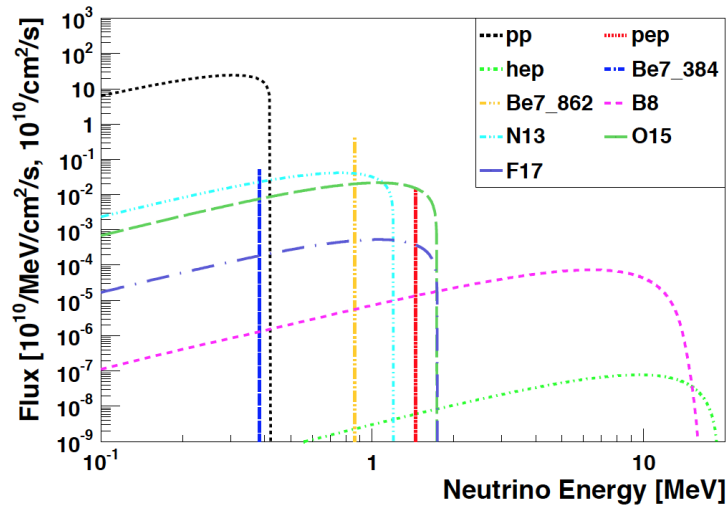
Figure 1.5   Solar neutrino flux spectra as a function of energy. The unit for all the continuum spectra is $10^{10}/\text{MeV}/\text{cm}^2/\text{s}$, while for line sources, the units is $10^{10}/\text{cm}^2/\text{s}$ [16].

1.2.1   Solar neutrino detectors

Historically, there were five major experiments to hunt for solar neutrinos such as Chlorine (^{37}Cl)[17] at Homestake, Gallium (^{71}Ga)[18,19], Kamiokande[20], SNO[21] and Borexino[22]. The first two experiments used the radiochemical technique to detect the solar neutrinos and the last three experiments adopted the techniques of water Cherenkov, heavy water and scintillation, respectively.

1.2.1.1   Chlorine (^{37}Cl) experiment

In 1960, Ray Davis[17] was the pioneer to detect the solar neutrinos at Homestake gold mine. He used 600 tons of C_2Cl_4 as the target material to search the neutrinos via the following chemical reaction,

$$\nu_e + {}^{37}\mathrm{Cl} \rightarrow {}^{37}\mathrm{Ar} + e^-. \tag{1-25}$$
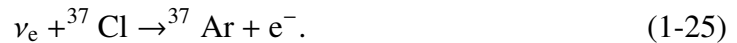
with 0.814 MeV energy threshold. The experiment had taken data for 30 years. Homestake reported the average solar neutrino flux is 2.56 ± 0.23 SNU (solar neutrino units, 1 SNU = 10^{36} per capture/atom/s), which was only 30% of the Standard Solar Model (SSM) prediction. This deficit raised the well known solar neutrino missing puzzle.

1.2.1.2   Gallium (^{71}Ga) experiment

By adopting gallium as a target material, one can reach a lower energy threshold of 0.214 MeV, which is sensitive to pp-chain neutrinos,

$$\nu_e + {}^{71}\mathrm{Ga} \rightarrow {}^{71}\mathrm{Ge} + e^-. \tag{1-26}$$

SAGE in Russia and GALLEX/GNO in Italy were this type of experiments. Both measured the average solar neutrino flux, SAGE reported $67.2^{+7.2+3.5}_{-7.0-3.0}$ SNU and GALLEX/GNO 69.3 ± 5.5 SNU, respectively. Both measurements were still half of the SSM and confirmed the solar neutrino missing puzzle raised by Homestake.

1.2.1.3   Kamiokande and Super-Kamiokande experiments

Kamiokande and Super-Kamiokande provided the real time observation in Kamioka (Japan), used pure water as a target material. The elastic scattering process

is used to detect the solar neutrinos, with the major contribution from,

$$\nu_e + e^- \rightarrow \nu_e + e^-. \tag{1-27}$$

Kamiokande reported the solar ν_e flux of ^{8}B is $(2.8 \pm 0.4) \times 10^6 (\text{cm}^{-2}\text{s}^{-1})$ and Super-Kamiokande reported $(2.35 \pm 0.08) \times 10^6 (\text{cm}^{-2}\text{s}^{-1})$, [20,23]respectively. The later provided a precise measurement because of using 50 kiloton pure water as its target. Both measurements were also significantly less than the prediction by SSM.

1.2.1.4   SNO experiment

SNO (Sudbury neutrino observatory) searched the solar neutrino using 1 kton heavy water as Cherenkov detector through three channels.

$$\text{Charge Current (CC)} : \nu_e + d \rightarrow p + p + e^-, \tag{1-28}$$

$$\text{Neutral Current (NC)} : \nu_x + d \rightarrow p + n + \nu_x, \quad (x = e,\ \mu,\ \tau), \tag{1-29}$$

$$\text{Elastic Scattering (ES)} : \nu_x + e^- \rightarrow \nu_x + e^-, \quad (x = e,\ \mu,\ \tau). \tag{1-30}$$

The ES channel is the same as that in Super-Kamiokande experiment. The measurements for the corresponding channels are[21]:

$$\phi_{\text{CC}} = \phi_{\nu_e} = \left(1.68^{+0.06+0.08}_{-0.06-0.09}\right) \times 10^6 \ (\text{cm}^{-2}\text{s}^{-1}), \tag{1-31}$$

$$\phi_{\text{ES}} = \phi_{\nu_e} + 0.155(\phi_{\nu_\mu} + \phi_{\nu_\tau}) = \left(2.35^{+0.22+0.15}_{-0.22-0.15}\right) \times 10^6 \ (\text{cm}^{-2}\text{s}^{-1}), \tag{1-32}$$

$$\phi_{\text{NC}} = \phi_{\nu_e} + \phi_{\nu_\mu} + \phi_{\nu_\tau} = \left(4.94^{+0.21+0.38}_{-0.21-0.34}\right) \times 10^6 \ (\text{cm}^{-2}\text{s}^{-1}). \tag{1-33}$$

Since SNO can measure the ν_e's, ν_μ's and ν_τ's, in which the last two are the neutrinos oscillated from the ν_e's and disappear in most of the solar experiments, and hence can give an unambiguous solution on the solar neutrino missing puzzle. The SNO measurement

on the sum of all the three flavour solar neutrinos agrees with the prediction by SSM, solving the long-standing problem of solar neutrino missing puzzle.

1.2.2 Remaining issues for solar neutrinos

Although the solar neutrino missing puzzle has been solved by the neutrino oscillations, there are still a number of issues related to solar neutrinos to be understood. The transition phase of solar neutrino oscillation from the vacuum to matter effect has not been experimentally confirmed yet. The CNO and *hep* neutrinos have not been observed. Even for the fluxes of *pp*, ^{7}Be, ^{8}B and *pep* neutrinos, precise measurements are still needed in order to improve the study of SSM and even the future study of neutrinoless double beta decay. All of which are expected to be significantly improved at China JinPing underground Lab (CJPL), the ideal underground facility with the largest overburden in the world.

From previous and ongoing solar neutrino experiments, all the backgrounds which significantly affect the study of solar neutrino experiments are known to be

1. Cosmogenic backgrounds, in which the β-ray from the radiative isotopes induced by cosmic spallation can mimic a solar neutrino event. These backgrounds at CJPL can be suppressed by 200 and 2 times in comparing with Borexino and SNO.

2. Internal radioactivity with β and γ-ray, which are very dangerous to the low background experiments. The effect can be minimized using the purification of the target material.

3. External background, which are mainly from the detectors construction material. This thesis will discuss the gamma radioactivity and provide measurements in Chapter 4.

1.3 Geoneutrinos

1.3.1 Brief history of geoneutrinos

In the mid of 1960's, Eder proposed an idea to explore the Earth by the study of antineutrinos[24], since these antineutrinos can be associated with the beta decays of radiative isotopes in the Earth. In 1984, Krause et al. extended the idea, and gave the estimation of geoneutrino flux and its detection[25]. After two decades of Kraus's estimation, in 2005, KamLAND was a pioneer to observe the existence of

geoneutrinos[26]. Later on, in 2010, Borexino also participated in this race and again confirmed the existence of geoneutrino from the Earth[27].

Since then, a number of geoneutrino studies have been performed. Using the measurements on geoneutrino fluxes at various locations can provide an insight to the mantle heat generated by radiative decays. This has not been addressed by any conventional geological method.

1.3.2   Current geoneutrino detections

The study of the Earth by geoneutrinos[28] is now only possible because of advances in technology that allows for larger neutrino detectors. The measurements already made by KamLAND (Fig. 1.6) and Borexino (Fig. 1.7)[26,27,29–31].

We will briefly explain the KamLAND and Borexino measurements, as below:

1.3.2.1   KamLAND

KamLAND detector was installed at Kamioka Observatory, initially for the study of the reactor neutrino oscillations, later used for geoneutrino detections and search for the neutrinoless double beta decay.

The site is enclosed with 53 nuclear reactor. The nearest reactor to KamLAND is 180 km. In 2011, due to the Fukushima accident, most of the reactors in Japan are shutdown, reducing more than 97% antineutrino flux at KamLAND, which becomes a good detector for detecting geoneutrinos[30].

As shown in Fig. 1.6, KamLAND used the liquid scintillator to detect the neutrinos from Earth and nuclear reactors. It has 1 kiloton target mass. The outer detector (OD) of KamLAND has been made by stainless steel (SST), having a diameter of 18m. 1879 PMTs are installed at inner lining, and each has a diameter of 50 cm. The Second inner layer filled with the other fluorescent and scintillation material. Non-scintillating material such as oil shields against external contaminations.

KamLAND has observed 116^{+28}_{-27} geoneutrinos from ^{238}U and ^{232}Th. This is equivalent to the geoneutrino flux of $(3.4 \pm 0.8) \times 10^6$ /cm^2/s[30].

1.3.2.2   Borexino

Borexino was designed for the low-level neutrino probes. Which is currently running at Gran Sasso, Italy. The major motivation of the experiment is to probe solar neutrinos,
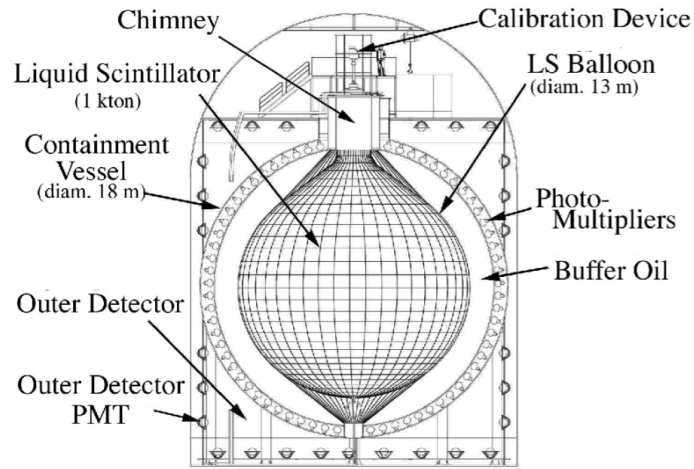
Figure 1.6   Layout of the KamLAND Detector[30].

especially for the mono energetic neutrinos, such as ^{7}Be EC neutrinos, through the electron scattering in the liquid scintillator. Layout of Borexino detector is shown in Fig. 1.7.
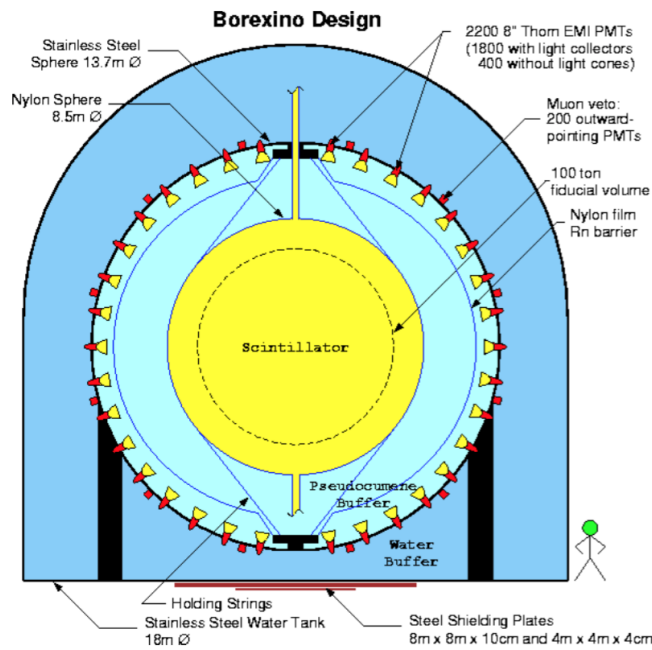
Figure 1.7   Layout of the Borexino detector[32].

Borexino has observed $23.7^{+6.5}_{-5.7}$(stats) $^{+0.9}_{-0.6}$(sys) geoneutrinos from ^{238}U and ^{232}Th. This was split into the geoneutrino flux from ^{238}U, which is $(2.7 \pm 0.7) \times 10^6$ /cm^2/s, and that from ^{232}Th, which is $(2.3 \pm 0.6) \times 10^6$ (/cm^2/s)[32].

1.3.3   Proposed geoneutrino detectors

Jiangmen Underground Neutrino Observatory (JUNO) is another exciting experiment under construction. The experiment will take data in 2020. JUNO[33] is 20 times more massive comparing to KamLAND and 60 times more massive comparing to Borexino.

SNO+ will start taking data in 2017[34]. Low Energy Neutrino Astronomy (LENA)[35], Deep Underground Science and Engineering Laboratory (DUSEL)[36], Baksan Neutrino Observatory (BNO)[37], Earth AntineutRino TomograpHy (EARTH)[38] and Hawaii Anti-Neutrino Observatory (Hanohano)[39] all are future planned experiments for neutrino searches including geoneutrinos.

The Jinping neutrino experiment is also another proposed experiment in China which is far away from the current and future planned nuclear reactor. The detector will be 4 times more massive than that of KamLAND. This experiment is expected online in 2022, see details in Chapter 5.

1.4   Low level background experiments

There are many low level background experiments are running around the world[40] and applied in different research fields, including double beta decay experiments[41].

Due to the nature of low-energy neutrinos, it indeed needs a very low level of background, then detectors can approach the required sensitives. Jinping underground neutrino experiment will be one of the lowest level background experiments in the world for the studies of solar, geoneutrino and others. Because of very small cross-section of low-energy neutrinos, all the backgrounds should be carefully studied. The contamination can be from either the detector material or the environment. A detailed study on the backgrounds is given in the Chapter 4.

1.5   Roadmap of this thesis

Chapter 3discusses the Jinping underground neutrino experiment's location, detector concept, and some unique features. This thesis will address two major topics: 1) measurement on the radiative background on the stainless steel for future experiment at Jiping in Chapter 4; 2) estimation of both the signal and background in a geoneutrino

at Jinping in Chapter 5. Fig.1.8, shows the issues to be studied and the connection among the radiative isotopes.
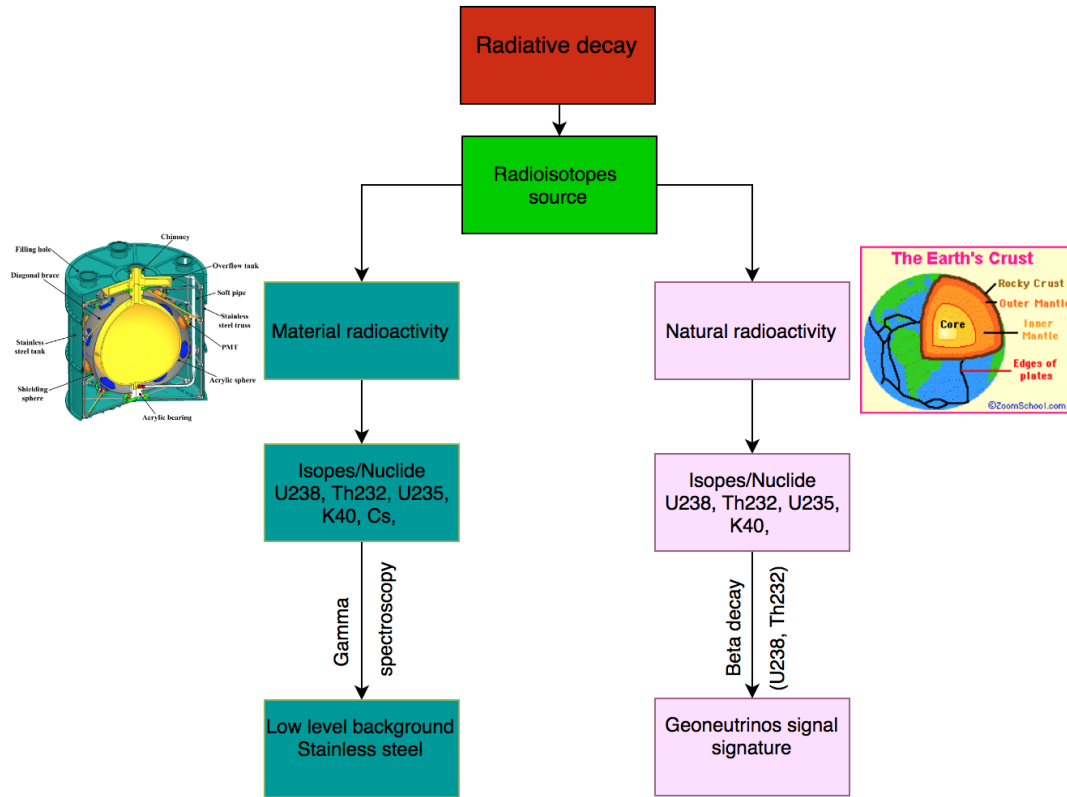
Figure 1.8   Issues to be studied and the connection among the radiative isotopes in this thesis. There are two types of radioisotopes: source, the cyan blocks indicate the possible Jinping detector material's contamination flow chart. We test the material by applying different methods to investigate the radioactivity in the detection material. The pink blocks indicate the flow chart for the production of geoneutrinos. From the top to the bottom, we have natural radioactivity present in our Earth's interior in the form of isotopes like ^{238}U, ^{232}Th, ^{235}U and ^{40}K, all of which appear as the background in the solar neutrino experiment. However, their radiative decays provides the geoneutrino that can be used for the studies of geo-science.

1.5.1 Stainless steel with a low level background (for future solar neutrino exp.)

Stainless steel (SST) with a low level background is needed in low-energy neutrino experiments. Several efforts have been made in the past few years to produce SST with the low level background [40,42]. SST is a key material in constructing a detector used in the detections of rare events such as ν interactions, e.g. solar neutrinos and geo-neutrinos.

Both neutrino signals are very sensitive to the low level radioactivity contamination. Proper material selections should be made with a close relation with the manufacturer and pinned down each step to achieve a low level background SST. For the production of such kind of SST, we must control the whole smelting procedure.

We selected a number of SST samples, including a raw iron sample, an ingot sample, two custom-made 304L and 316L samples, two commercial 304L and 316 samples. We carried out radioactive measurements on these samples individually on surface and underground. We compared our results with other low level background experiments in Chapter 4.

1.5.2   Signal and background signature of Geo-neutrino

Geo-neutrinos ($\bar{\nu}_e$'s) are produced from the natural radioactive decay of ^{238}U, ^{232}Th, and ^{40}K in the Earth; and providing interior information about it. The low-energy neutrino experiment at CJPL will have incredible features such as: low muon, low reactor flux and low rock radioactivity. We will study the radioactive nucleus decay chains in the investigation on both the radioactive background for solar neutrino signal and the radioactive decays for geoneutrino signal. Because neutrinos can oscillate, we will also apply the oscillation theory to the evaluation of reactor background and the prediction of geoneutrino flux at CJPL in Chapter 5.

Chapter 2   Radioactive nucleus decay

Radioactive nucleus decay is the spontaneous process, in which unstable nuclide loses its identity or energy through a number of radiations, for example, alpha (α) radiations, beta (β^-) radiations associated with antineutrinos ($\bar{\nu}_e$'s) or neutrinos (ν_e's) in the result of electron capture (EC), gamma (γ) radiations via radiative transitions in nuclei. Any material having this type of unstable isotopes/nuclide is supposed to be radioactive.

2.1   Types of decays

This thesis will focus on three major types of decays relevant to the study of solar neutrinos and geoneutrinos.

2.1.1   Beta decay

Beta decay, as what the name is called, is a decay with an electron and positron (historically they were referred as to beta particles) appearance in the final state. There are three major modes:

Beta-minus decay   happens in neutron rich isotopes/nuclides, as shown in Eq. (2-1),

$$
{}^{A}_{Z}X_N \rightarrow {}^{A}_{Z+1} X'_{N-1} + e^- + \bar{\nu}_e, \tag{2-1}
$$

with a negative charge particle (electron) and an electron antineutrino produced in the final state.

Beta-plus decay   occurs in proton rich isobars, as shown in Eq. (2-2),

$$
{}^{A}_{Z}X_N \rightarrow {}^{A}_{Z-1} X'_{N+1} + e^+ + \nu_e, \tag{2-2}
$$
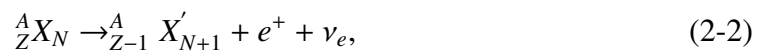
with a positive charge beta particle (positron) and an electron neutrino in the final state.

Electron capture (EC)   occurs in neutron-poor nuclides, as shown in example Eq. (2-3),

$$_{Z}^{A}X_N + e^- \rightarrow _{Z-1}^{A} X^{'} + \nu_e, \tag{2-3}$$
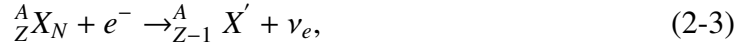
and also with the practical example of ^{40}K nuclide that has two decay modes: one is the beta minus decay with $4\bar{\nu}_e$'s 's emitted in the final state, as shown in the top of Eq. (2-4) and; the other is the EC process as shown in the bottom of Eq. (2-4), respectively.

$$^{40}\text{K} \rightarrow ^{40}\text{Ca} + e^- + 4\bar{\nu}_e + 1.311 \text{ MeV} \quad (89.3\%),$$
$$^{40}\text{K} + e^- \rightarrow ^{40}\text{Ar} + \nu_e + 1.505 \text{ MeV} \quad (10.7\%). \tag{2-4}$$
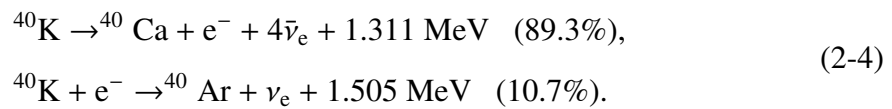
2.1.2   Gamma decay

Shown in Fig. 2.1, a nucleus changes from an excited to a lower energy state via an emission of the gamma radiation (also known as electromagnetic radiation).
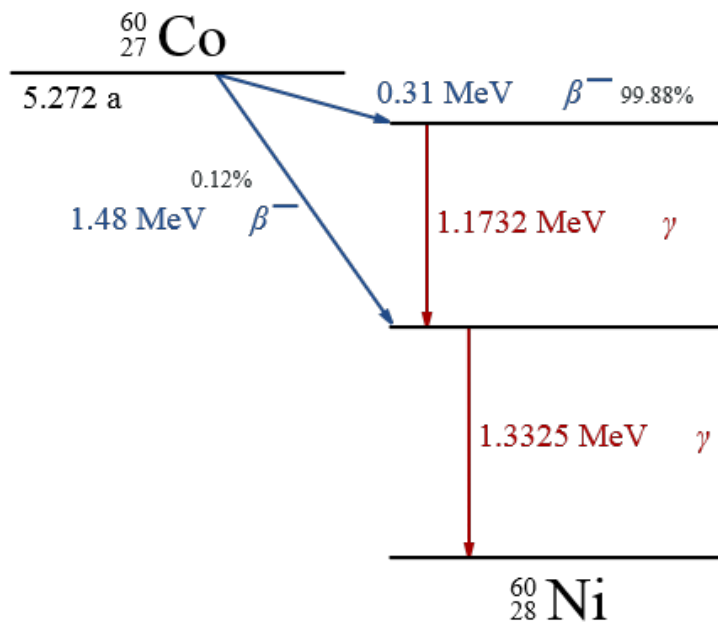
Figure 2.1   The radioactive decay levels of ^{60}Co, which mainly decays to nickel via a β^--decay, and then transits to two more stable nickel nuclei via two further gamma emissions.

In this process, no change occur in the number of protons(and neutrons), thus the parent and daughter nuclide have the same chemical composition. In this process, the

recoiling nucleus and emitted gammas (photons), both have a feature of monochromatic energy after the decay.

2.2   Angular momentum and parity in beta decay

For a common beta decay

$$^A_Z X_N \rightarrow ^A_{Z+1} X'_{N-1} + e^- + \bar{\nu}_e. \tag{2-5}$$

The conservation of angular momentum requires

$$\vec{I}_i = \vec{I}_f + \vec{S} + \vec{L}, \tag{2-6}$$

where $\vec{I}_i$ and $\vec{I}_f$ are the parent and daughter nucleus spin angular momentum, respectively. $\vec{S}$ and $\vec{L}$ represent the spin and orbital angular momentum of the two-lepton system, in which

$$\vec{S} = \vec{S}_e + \vec{S}_\nu, \tag{2-7}$$

where $\vec{S}_e$ and S_ν are the spins of electron and neutrino, respectively. Commonly, β decay can be divided into two transitions, allowed ($L = 0$) and forbidden transitions ($L \neq 0$).

- Allowed transition: In Gamow-Teller transitions, the spin of the emitted nuclide couples to the total spin of the two-lepton system with $S = 1$, in which the direction of electron spin is parallel to that of the electron antineutrino and, $I_i = I_f+1$, I_f, I_f-1. In case of Fermi transition, the spin of the emitted nuclide couples to the total spin of the two-lepton system with $S = 0$, in which the spins of the two leptons are anti-parallel and, $I_i = I_f$. The spins of parent and daughter's nuclides are the same. The corresponding selection criteria can be written as:

$$\Delta I = I_i - I_f = 0, \pm 1, \tag{2-8}$$

where ΔI represents the change the nucleus spin in the initial and final states. Even though the parity is not conserved in beta decays, one can still treat it as a conservative quantity if the beta decays are in the non-relativistic case, so that the parity change of the nuclides can be regarded as the orbital parity carried away by

the leptons, namely

$$\pi_i = \pi_f(-1)^L, \tag{2-9}$$

where π_i and π_f are the parities of the nuclides in the initial and final states, respectively. While L is the value of orbital angular momentum carried away by the leptons. Therefore, the selection criteria on the parity of nuclide is

$$\Delta\pi = \pi_i\pi_f = (-1)^L. \tag{2-10}$$

Apparently, for allowed beta decays with $L = 0$，one has

$$\Delta\pi = +1. \tag{2-11}$$

- Forbidden transitions: leptons in the final state take away the orbital angular momentum, where $L \neq 0$. The forbidden transition can be classified into different levels, e.g. $L = n$, where n is for the n-th forbidden transition level. the corresponding selection criteria are,

$$\Delta I = \pm n, \pm(n + 1). \tag{2-12}$$

According to Fermi's Second Golden Rule, the transition probability λ is,

$$\lambda = \frac{2\pi}{\hbar}|H_{fi}|^2 n_f(E_f), \tag{2-13}$$

where λ is the transition probability, $|H_{fi}|^2$ is the Hamiltonian matrix element, $n_f(E_f)$ is the density of the final states. Forbidden transition can be further divided into two sub categories: unique forbidden transition and non-unique forbidden tradition. Unique forbidden decays can be represented as:

$$\Delta I = \pm n,$$
$$\Delta\pi = (-1)^n. \tag{2-14}$$

Non-unique forbidden decay can be represented as:

$$\Delta I = \pm(n + 1),$$
$$\Delta\pi = (-1)^n. \tag{2-15}$$

2.3   Units and variables

It is convenient to write the total energy of the electron W, in term of the rest energy of electron ($m_e c^2$), since

$$W = \frac{m_e c^2 + T_e}{m_e c^2} = 1 + \frac{T_e}{m_e c^2}, \tag{2-16}$$

where T_e is the kinetic energy of electron. Assuming the mass of neutrino to be zero, then one can have the maximum energy of electron to be

$$W_o = 1 + \frac{Q}{m_e c^2}, \tag{2-17}$$

where $Q = T_e + T_\nu$. According to the relativistic energy relationship, the energy of electron is

$$E_e^2 = p^2 c^2 + (m_e c^2)^2, \tag{2-18}$$

so

$$W^2 = p^2 + 1. \tag{2-19}$$

Where p is the electron momentum and has a unit of $m_e c$ in Eq. (2-19).

2.4   Allowed transition energy spectrum

The energy spectrum of the allowed β[43] decay can be written as

$$N(W)_{\mp} dW = \frac{g^2}{2\pi^3} \xi p W (W_o - W)^2 dW, \tag{2-20}$$

where g is the weak charge, while ξ is the nuclear matrix. The decay constant of beta decay is

$$\begin{aligned}
\lambda = \frac{ln2}{T_{\frac{1}{2}}} &= \int_1^{W_o} N(W) dW, \\
&= \frac{g^2}{2\pi^3} \xi \int_1^{W_o} p W (W_o - W)^2 dW.
\end{aligned} \tag{2-21}$$

Let the integral to be

$$f = \int_1^{W_o} p W (W_o - W)^2 dW, \tag{2-22}$$

then the comparative half-lives ft is given by

$$ft = fT_{\frac{1}{2}} = \frac{ln2}{g^2\xi/2\pi^3},$$
(2-23)

which can be measured by experiments. We know that, it is only related to the nuclear matrix elements. So the allowed transition formula can be written as:

$$N(W)_{\mp}dW = \frac{ln2}{ft}pW(W_o - W)^2dW.$$
(2-24)

2.5   Forbidden transition energy spectrum

2.5.1   General energy spectrum formula

The forbidden β-decay[44] transition can be written as:

$$N(W)_{\mp}dW = \frac{g^2}{2\pi^3}S_n(\pm Z, W)pW(W_o - W)^2dW,$$
(2-25)

where $S_n(\pm Z, W)$ is the shape factor for the n-th levels. Since the leptons take away the angular momentum, the probability of beta particle with the same energy is reduced, the spectrum profile will be distorted in comparing to the allowed decays. $S_n(\pm Z, W)$[43] is used to describe the change and can be written as below:

$$S_n^{J\geq 1} = \frac{8\pi(J-1)!R^{2(J-1)}}{(1+\gamma_0)(2J-1)!!}\sum_j \frac{(2j)!!}{(2J-2j)!!}\frac{L_{j-\frac{1}{2}}q^{2(J-j)-1}}{(j-\frac{1}{2})!(J-j-\frac{1}{2})!}\mathcal{M}_j^2(J),$$
(2-26)

in which Z is the number of protons in the β decay. $j = \frac{1}{2}, \frac{3}{2}, ..., J - \frac{1}{2}$, where J is the difference of nuclear spin angular momentum between the initial and final state ΔI. $L_{j-1/2}$ is proportional to the electron radial wave function in the nucleus. Treating the nucleus as point charge gives

$$L_{k-1} \approx \frac{1}{2}(2p)^{2(\gamma-\gamma_0)}\left[\frac{\Gamma(2\gamma_0+1)}{\Gamma(2\gamma+1)}\right]^2|\frac{\Gamma(2\gamma+iv)}{\Gamma(\gamma_0+iv)}|^2k(k+\gamma).k = J + 1/2,$$
(2-27)

where $\gamma = [k^2 - (\alpha Z)^2]1/2$, $v = \pm\alpha ZW/p$. $\mathcal{M}_j(J)$ only relates to the nuclear matrix elements, and has different forms in the unique and non-unique forbidden decays.

2.5.2   Unique forbidden channels

In the unique forbidden channels $J = \Delta I = n + 1$ the forbidden transition shape factor can be written as

$$S_n^{n+1} = \frac{8\pi n! R^{2n} \mathcal{M}^2 (n+1)}{(1+\gamma_0)(2n+1)!!} \sum_k \frac{(2k-1)!!}{(2n-2k+3)!!} \frac{L_{k-1} q^{2(n-k+1)}}{(k-1)!(n-k+1)!}, \qquad (2\text{-}28)$$

2.5.3   Non-unique forbidden channels

In the non-unique forbidden channels, $J = \Delta I = n^{[43]}$ the forbidden shape factor can be written as:

$$S_n^n = \frac{8\pi (n-1)! R^{2n-1} \mathcal{M}^2 (n)}{(1+\gamma_0)(2n-1)!!} \sum_k \frac{(2k-1)!!}{(2n-2k+1)!!} \frac{L_{k-1} q^{2(n-k)}}{(k-1)!(n-k)!}. \qquad (2\text{-}29)$$

2.6   Corrections

In the preceding two sections, we have discussed the allowed and forbidden transition energy spectra. We now apply different kinds of corrections such as Coulomb, screening, finite-size electromagnetic, and finite-size weak interaction correction, respectively.

2.6.1   Coulomb correction (Fermi correction)

The Coulomb correction can be described by the Fermi function $F(\pm Z, W)^{[43,44]}$ and is applicable for both the allowed and forbidden transition, especially at the low energy level, when the nucleus is treated as a point charge. Due to the Coulomb attraction the electron is decelerated and the positron is accelerated due to the Coulomb repulsion as shown in Fig. 2.2.

$$F(\pm Z, W) = 2(1+\gamma_0)(2pR)^{-2(1-\gamma_0)} e^{\pi v} \frac{|\Gamma(\gamma_0 + iv)|^2}{|\Gamma(2\gamma_0 + 1)|^2}, \qquad (2\text{-}30)$$

where

$$\gamma_0 = [1 - (\alpha Z)^2]^{1/2}, \qquad (2\text{-}31)$$

$$\alpha = \frac{e^2}{\hbar c} = \frac{1}{137.03599}, \qquad (2\text{-}32)$$

23
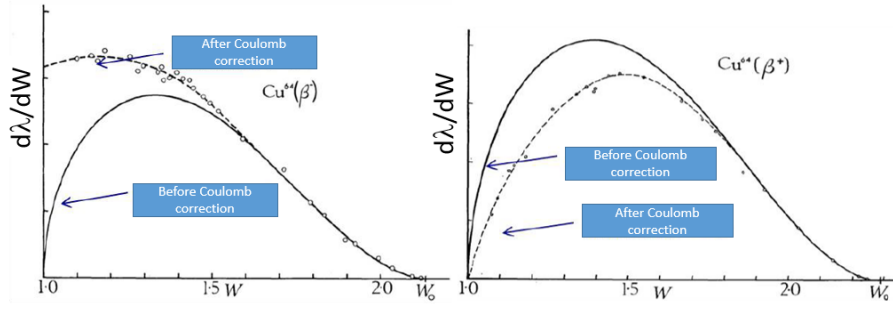
Figure 2.2   (Left side) β^- decay and the right side β^+ decay, before and after the Coulomb correction, respectively[45].

$$v = \pm \frac{\alpha Z W}{p}, \tag{2-33}$$

where Z is the atomic number. The sign is '+' for the β^+ decay, while it is '-' for the β^- decay. R is the daughter's radius, according to Elton formula, it is

$$R = 0.0029 A^{1/3} + 0.0063 A^{-1/3} - 0.017 A^{-1}. \tag{2-34}$$

2.6.2   Screening correction

$S(Z, W)$[46] accounts for the screening correction of the nucleus charge by the e^- in the atomic bound state and it effectively reduces the charge seen by the electron. The screen correction can be written as:

$$F'(\pm Z, W) = F(\pm Z, W \pm V_0) \left[\frac{(W \pm V_0)^2 - 1}{W^2 - 1} \right]^{1/2} \left(\frac{W \pm V_0}{W} \right), \tag{2-35}$$

where V_0 is the screening potential and can be derived by the numerical calculations of

$$V_0 = N(\tilde{Z}) \alpha^2 \tilde{Z}^{\frac{4}{3}}, \tag{2-36}$$

where $\tilde{Z}$ and Z indicate the number of protons in parent and daughter, respectively. The practical example of screening correction is shown in Fig. 2.3.

2.6.3   Finite-size correction

The actual nucleus, having a finite size, charge and hypercharge distribution, cannot be treated as a point charge. So that the electromagnetic and weak interactions are no longer considered to occur in the central potential field during the β decay, and needed

to be modified separately, denoted as Finite Size EM and Finite Size WI corrections. It is usually considered that the charge and hypercharge in the nucleus are uniformly distributed.

According to Ref.[47], the total correction effect of Finite Size EM towards a β decay spectrum should be shown as a multiplication factor, regarded as $L_0(Z, W)$.

For β^- decay, it is

$$
\begin{aligned}
L_0(Z, W) =& 1 + 13\frac{(\alpha Z)^2}{60} - WR\alpha Z\frac{41 - 26\gamma}{15(2\gamma - 1)} - \alpha ZR\gamma\frac{17 - 2\gamma}{30W(2\gamma - 1)} \\
& + a_{-1}\frac{R}{W} + \sum_{n=0}^{5} a_n(WR)^n + 0.41(R - 0.0164)(\alpha Z)^{4.5}.
\end{aligned}
\tag{2-37}
$$

For β^+ decay, it is

$$
\begin{aligned}
L_0(Z, W) =& 1 + 13\frac{(\alpha Z)^2}{60} - WR\alpha Z\frac{41 - 26\gamma}{15(2\gamma - 1)} + \alpha ZR\gamma\frac{17 - 2\gamma}{30W(2\gamma - 1)} \\
& + a_{-1}\frac{R}{W} + \sum_{n=0}^{5} a_n(WR)^n + 0.22(R - 0.0164)(\alpha Z)^{4.5}.
\end{aligned}
\tag{2-38}
$$

According to Ref.[47], the total correction effect of Finite Size WI towards a β decay spectrum should be shown as the factor $C(Z, W)$

$$
C(\pm Z, W) = 1 + C_0 + C_1 W + C_2 W^2,
\tag{2-39}
$$

where

$$
\begin{aligned}
C_0 &= \frac{-233}{630}(\alpha Z)^2 - \frac{(W_0 R)^2}{5} \pm \frac{2}{35}W_0 R\alpha Z, \\
C_1 &= \pm\frac{21}{35}R\alpha Z + \frac{4}{9}W_0 R^2, \\
C_2 &= \frac{-4}{9}R^2.
\end{aligned}
\tag{2-40}
$$

Here Z is the number of protons in the daughter nucleus. The practical example of finite-size correction is shown in Fig. 2.3.

2.6.4 Weak magnetism correction

The phenomena of weak magnetism was proposed by Gell-Mann. It is usually assumed that the nucleus is at rest state during the β decay. Due to the nucleus recoiling effect, the Coulomb field will change, and a correction for the electromagnetic effect of

the electrons from the decay is needed. According to Ref.[48], the weak magnetism can roughly describe the recoiling effect and can be written as

$$1 + \delta_{WM}W. \tag{2-41}$$

According to the approximation, $\delta_{WM} = (0.48 \pm 0.47)\% m_e$ is irrelevant to the number of protons Z[48]. The practical example of weak magnetism correction is shown in Fig. 2.3.
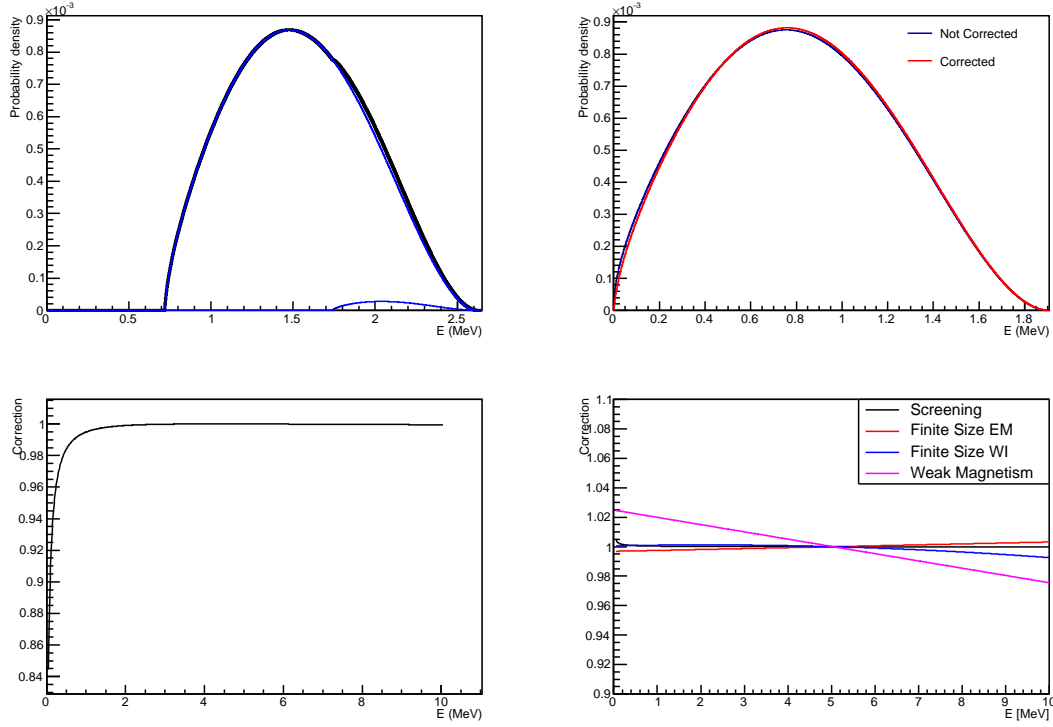
Figure 2.3   The β spectra (top), Coulomb and other corrections (bottom) for ^{10}C.

2.7   Corrected β spectra

According the discussion in the preceding Sections 2.4-2.6, the corrected beta decay spectrum can be written as:

$$N(\pm Z, W) \mp dW = KpW(W_0 - W)^2 F(\pm Z, W)S_n(\pm Z, W)$$
$$\times S(\pm Z, W)L_0(\pm Z, W)C(\pm Z, W)M(W)dW. \tag{2-42}$$

where $S(\pm Z, W)$ indicates the screening effect, $L_0(\pm Z, W)$ indicates the finite-size EM, $C(\pm Z, W)$ indicates finite-size weak interaction and $M(W)$ indicates the weak magnetism correction, respectively.

The corrected β spectra can be further divided into two portions, to study the solar neutrino background and geoneutrino signal.

2.7.1   Solar neutrino background

With the corrected beta decay spectrum, we can use this equation to plot the solar neutrino background. In solar neutrino, there are two kinds of background, cosmogenic and residual radioactivity.

An example decay level of ^{85}Kr is shown in Fig. 2.4,
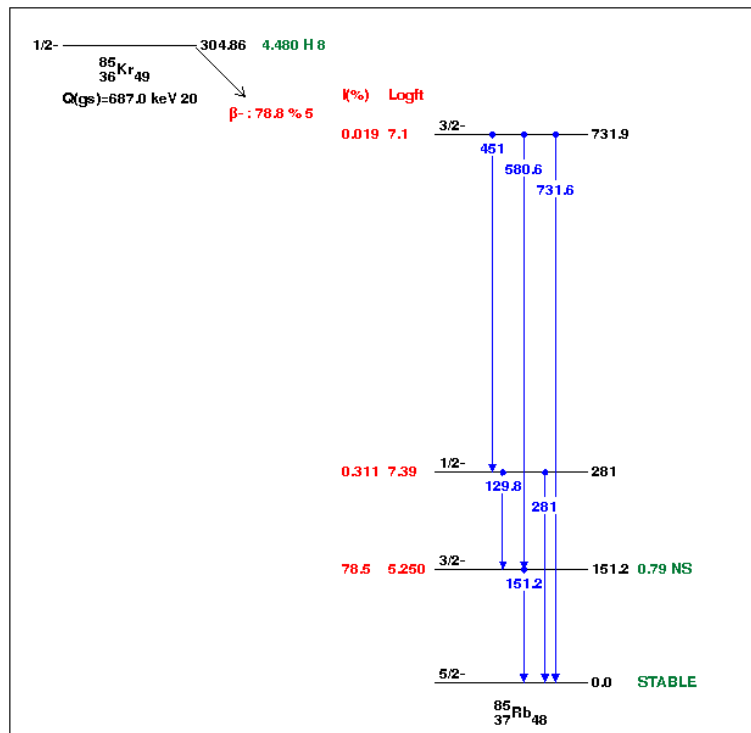
Figure 2.4   The decay scheme of ^{85}Kr (Figure taken from www.nndc.bnl.gov).

The detailed backgrounds for solar neutrinos can be seen in Fig. 2.5 with corrections. Each blue curve gives the contribution from individual branch, and the black curves are for the total of each branch after applying the corrections. All these 8 radiative isotope decay can produce beta's and gamma's with energy close to the energy of electron ejected by the solar neutrino scattering in matter.

2.7.2   Geoneutrino signal

Geoneutrinos are from the beta decays of three major isotopes ^{238}U, ^{232}Th, and ^{40}K. Unlike those radioactive isotopes in the study of solar neutrinos, these three isotopes
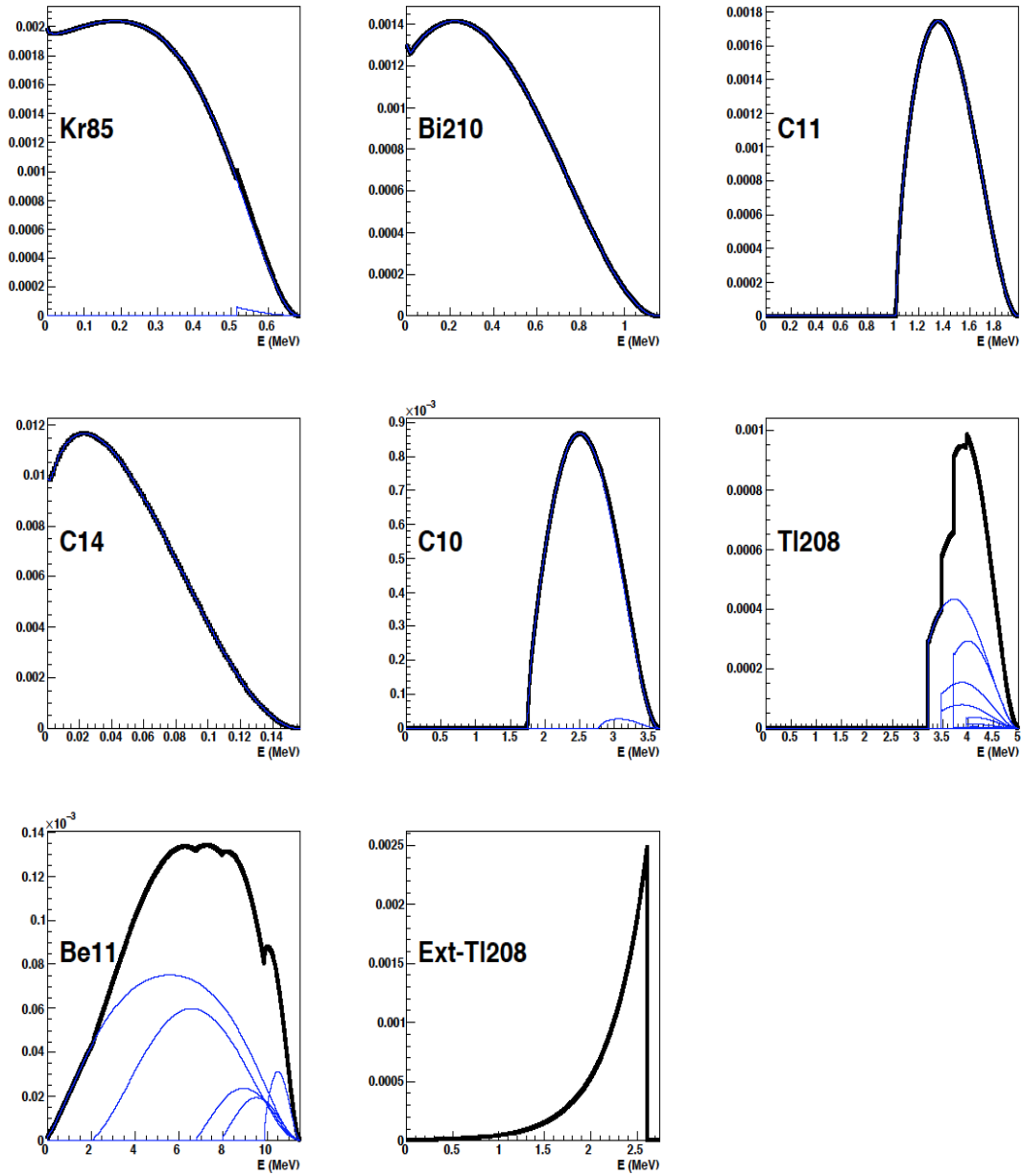
Figure 2.5   The energy spectra (black) for radiative backgrounds in the experimental study of solar neutrinos. The contribution from the individual branch is also in the blue curve. From left to right, first seven spectrums of residual radiative and cosmogenic background[16].

produce the geoneutrinos, which serve as a probe to the radiative heat generated in the Earth. Taking ^{238}U as an example, we give the beta spectra and the relevant corrections. Among the ^{238}U isotopes, the major contributions to the intensity of the geoneutrino are from the beta decays of ^{234}Pa$_m$ and ^{214}Bi as shown in Table 2.1. ^{232}Th also shown in Table 2.2.

For the case of geoneutrinos, the β spectra do not need to use all the nuclear

Table 2.1   Effective transition of ^{238}U[49]. Some of the nuclides, may decay into more than one channel, but for geoneutrinos β^- decay mode is required. The intensity of each individual decay level is mentioned. The detailed description of the allowed and the forbidden decays in the preceding Sections 2.2 and 2.5.1.

Isotope	Decay mode	E_{max} [keV]	Intensity	Type
^{234}Pa$_m$ → ^{234}U	β^-	2268.92	0.9836	1st forbidden
^{214}Bi → ^{214}Po	β^-	3272.00	0.182	1st forbidden
		2662.68	0.017	1st forbidden
		1894.32	0.0743	1st forbidden
		1856.51	0.0081	1st forbidden

Table 2.2   Effective transition of ^{232}Th[49]. Some of the nuclides, may decay into more than one channel, but for geoneutrinos β^- decay mode is required. The intensity of each individual decay level is mentioned. The detailed description of the allowed and the forbidden decays in the preceding Sections 2.2 and 2.5.1.

Isotope	Decay mode	E_{max} [keV]	Intensity	Type
^{212}Bi → ^{212}Po	β^-: 0.6406	2254	0.8658	1st forbidden
^{228}Ac → ^{228}Th	β^-: 1.0000	2069.24	0.06	Allowed
		1940.18	0.008	Allowed

corrections except for Coulomb and forbidden shape correction. After applying the forbidden correction, one can have the corrected spectra shown in Figure 2.6.
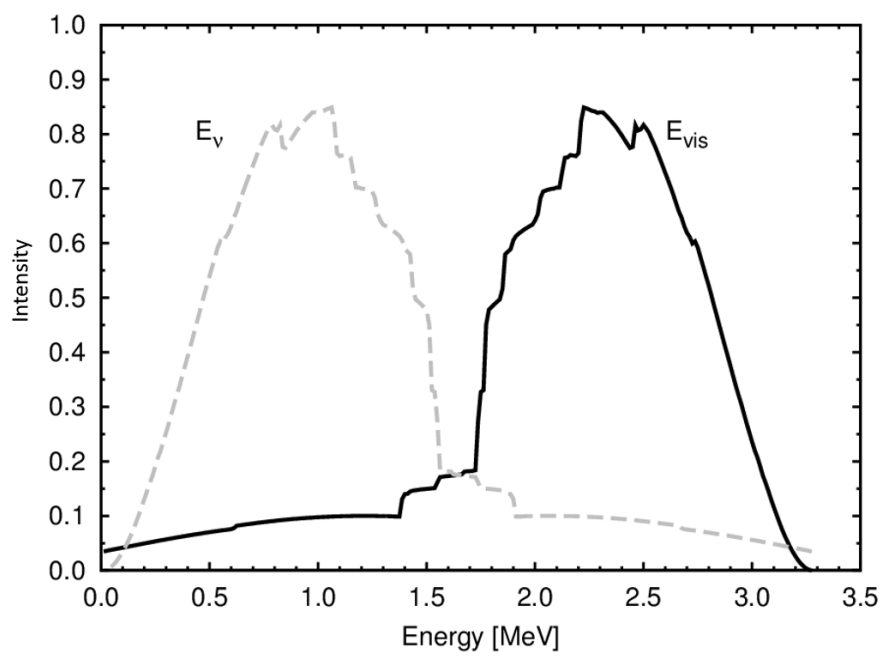
Figure 2.6   The β and antineutrino spectra of ^{214}Bi $^{[49]}$.

Chapter 3   China Jinping Underground Laboratory

The China Jinping underground Laboratory (CJPL)[50] is one of the world's ideal sites to perform low background neutrino experiments. The Jinping experimental site is located in Jinping Mountain, Sichuan, China as indicated in Fig. 3.1. The altitude of Jinping mountain is 4,100~4,500 meters and is surrounded by Yalong river. A 150-km river bend surrounds the mountain with a water level differences of 312 m between both sides. Jinping II Hydropower station was built by the China Yalong River Hydropower Development Company. Four head race tunnels, two traffic tunnels and one drainage tunnel were built to across the Jinping Mountain as shown in Fig. 3.2. The headrace tunnels measure 16.7 km in length and 12.4-13.0 m in diameter, with a maximal overburden around 2400 m[16].

Figure 3.1   China Jinping Underground Laboratory map. In the left-side map, the position of Jinping lab is marked and in the right-side map, the solid blue line indicates that Jinping lab is surrounded by the Yalong river and the blue dotted line represents the position of tunnels. There is only two-hour drive to CJPL from Xichang airport[16].

The Yalong River is situated in the geomorphological level II stepping stool of the move zone from Tibetan Plateau to Sichuan Basin. The elevation diminishes from around 5000 m in the northwest to roughly 2000 m in the southeast. The Jinping Mountain reaches out along an almost N-S direction[16].
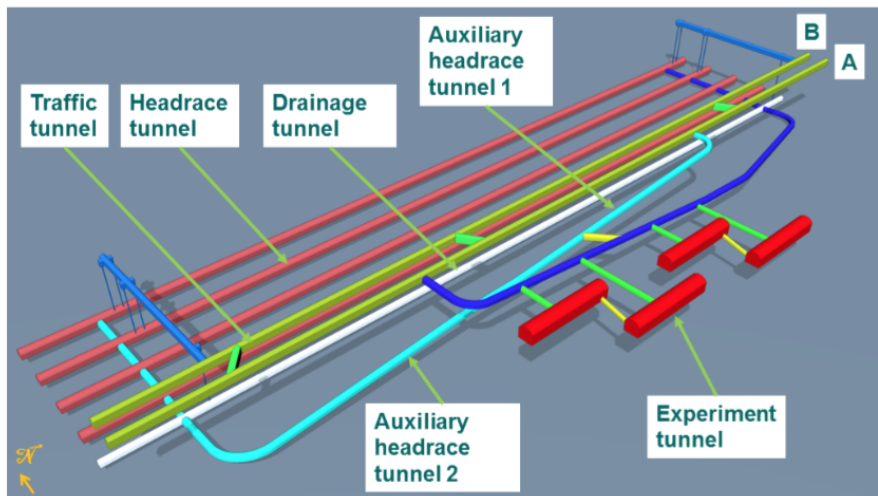
Figure 3.2   The overview of phase-II labs in CJPL[16].

3.1   Unique features of CJPL

CJPL has many incredible features. Only few of them are discussed below, especially for those related to the neutrino probes such as, rock radioactivity contamination, muon flux, distances to all the running or planned reactors:

3.1.1   Lowest rock radioactivity

The rock radioactive contamination has been measured in CJPL and discussed in Ref.[41]. CJPL was found to have the lowest rock radioactivity level among the present underground labs used for low-energy neutrino experiments. Table 3.1 shows a comparison with other experiments.

Table 3.1   CJPL rock radioactivity comparison with other underground facilities.

Site	^{238}U	^{232}Th	^{40}K	Reference
	Bq/kg	Bq/kg	Bq/kg	
Jinping	1.8±0.2 (^{226}Ra)	<0.27	<1.1	[41]
Sudbury	13.7±1.6	22.6±2.1	310±40	[51]
Gran sasso hall A	116±12	12±0.4	307±8	[52]
Gran sasso hall B	7.1±1.6	0.34±0.11	7±1.7	[52]
Gran sasso hall C	11±2.3	0.37±0.13	4±1.9	[52]
Kaminoka	~12	~10	~520	[53]

3.1.2 Lowest muon flux

Cosmic ray muons can interact with atoms, generating spallation products that are dangerous for low energy neutrino experiments. The resulting correlated or uncorrelated β- and γ-rays can form a pair of prompt and delay events, and thus mimicking the IBD events. The background produced by the muons can be rejected by introducing a large buffer and a long veto time window, which will cause a significant loss of detection efficiency. Muon flux depends upon the depth of the overburden. The muon flux at CJPL was measured to be as low as $2.0 \pm 0.4 \times 10^{-10}/(\text{cm}^2 \cdot \text{s})$[54]. Fig. 3.3 shows a comparison with other underground labs. The detail results regrading the muon related background in the detection of geoneutrinos are discussed in the Chapter 5.
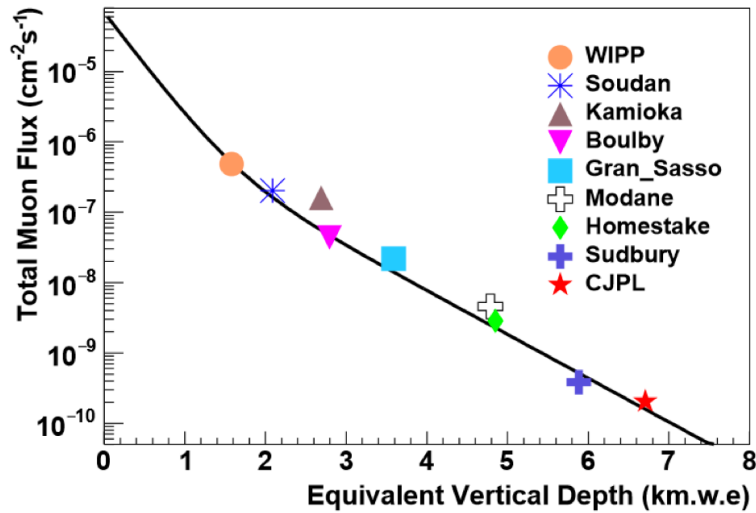
Figure 3.3   Total muon flux vs. Equivalent vertical depth in water. CJPL is the one of the deepest lab. in the world with a very low muon flux as comparing to the other facilities[16].

3.1.3 Lowest reactor antineutrino flux

The major man-made background for geoneutrino experiments are nuclear reactors. The detail results regrading the man-made background in the detection of geoneutrinos are discussed in the Chapter 5. Jinping is far from all the nuclear reactor power plants in operation or under construction. The nearest reactor to Jinping is ~950 km. Figure 3.4 shows all current nuclear reactors around the world. Also plotted are proposed Jinping underground neutrino site, and the ongoing low-energy neutrino experiments such as Borexino and KamLAND.
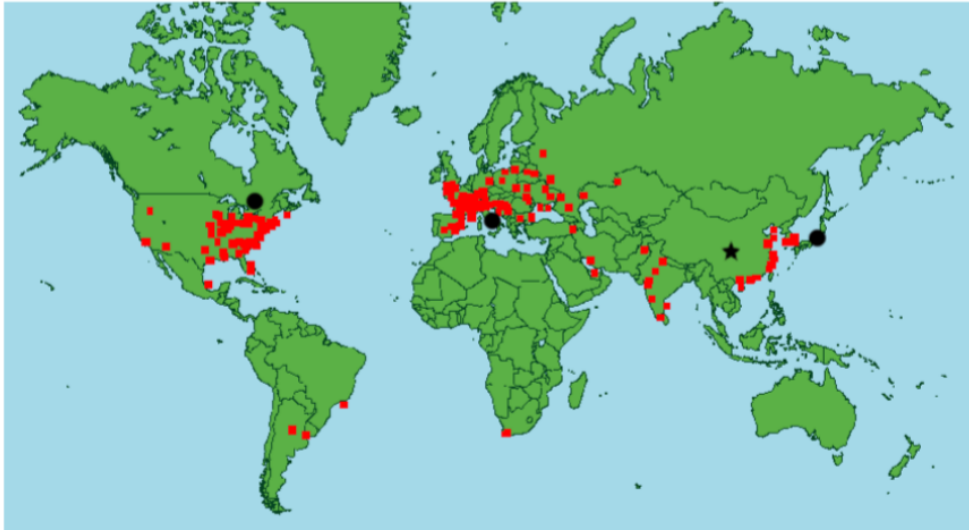
Figure 3.4   World map with all currently operational and planned nuclear power plants. The SNO, Gran Sasso, Kamland and Jinping sites are also marked[16].

3.2   Overview of the proposed Jinping neutrino experiments

As shown in Fig. 3.5, two caverns are used to host the two neutrino detectors. The dimensions of each cavern is 20×20 metres in height and diameter. The Jinping neutrino experiment is planned to install two detectors at CJPL II, by using the LS or slow liquid scintillaor[55] as a detection material. Each detector has a capacity of 1 kt of fiducial mass for solar neutrino probes, which is ~1.5 kt for supernova and geo-neutrino studies.

3.2.1   Detector concept

Figure 3.6, illustrates the conceptual design of detector in a cylindrical shape or a spherical shape. The height and diameter of central acrylic vessels are 20 meters in both spherical and cylindrical neutrino detectors. Three types of target materials are considered for the detection, liquid scintillator(LS) or water-based liquid scintillator (WbLS) at present are being considered as a target material. For the sphere inner vessel, the fiducial volume is a sphere of 12.8 m diameter, so that each neutrino detector can give 1 kiloton fiducial mass assuming the target material density to be 0.9 g/cm^3. For the cylinder inner vessel, it measures cylinder of 11.2 m in diameter and 11.2 m in height, and the fiducial mass is also 1 kiloton under the same density.
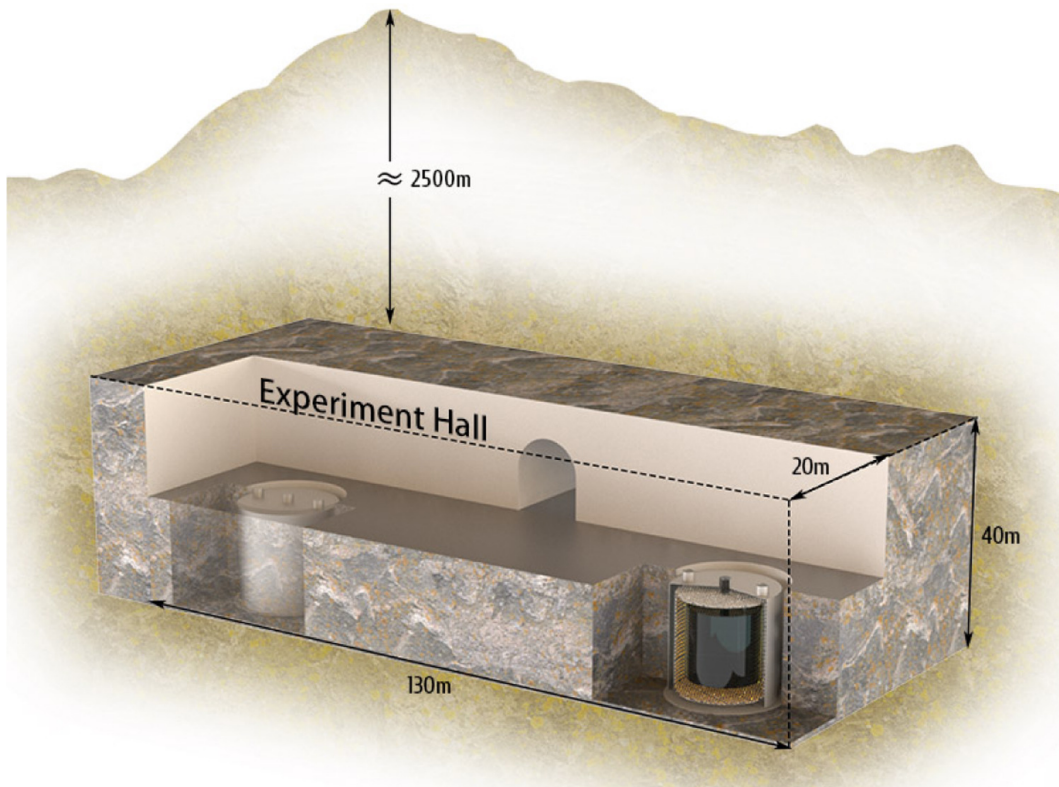
Figure 3.5   Overview of Jinping underground experimental hall[16].
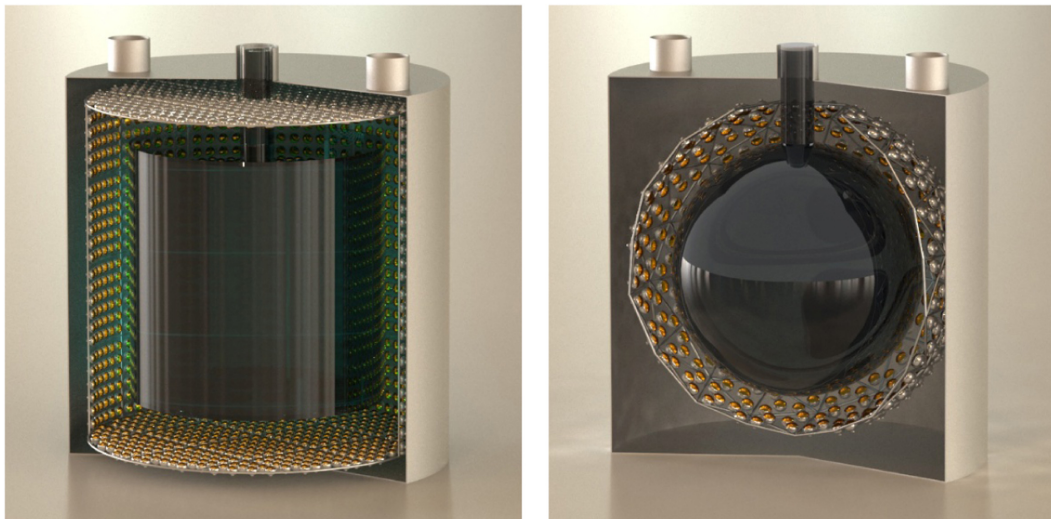
(a) Cylindrical scheme

(b) Spherical scheme

Figure 3.6   Jinping neutrino experiment detector schemes[56]. Two proposed detector layouts, where **(a)** is cylindrical and **(b)** is spherical. See the details in the text Sec. 3.2.1.

Chapter 4   Tests of stainless steel samples

Low-energy neutrino experiments require a very low background environment. In this thesis we focus on the background from the radioactive isotopes in the stainless steel (SST), which is going to be used to construct the neutrino detector. Several efforts have been made in the past few years to produce the low background level SST[40,42] for low background experiments. SST is a key material in today's detector's construction, and it is involved in the detections of rare events such as ν interactions, for solar neutrino and geoneutrino physics study.

To measure the radioactivity in SST, we selected a number of SST samples and semi-finished iron samples, which includes a raw iron sample, an ingot sample, two custom-made SST 304L and 316L samples and two commercial 304L and 316L samples.

4.1   Stainless steel samples

Stainless steel (SST) is an essential material in building a neutrino detector. Since the energy of solar neutrinos and geoneutrinos ranges from 0 to about 16 MeV, which is overlapped with the energy of β- and γ-rays from radioactive nucleus decays, a careful production and selection of SST is needed. However, each supplier or manufacturer has it's own specifications to produce the SST, which is probably not suitable to the low background experiments. So, we investigated the smelting process to produce low background SST assay. The chemical composition of different grades of SST can be seen in Table 4.1.

Commonly the smelting process done in MgO crucible in a vacuum chamber with an iron ingot mould. Cleanliness is the major part of the smelting process and were checked in each step or each alloy. No other impurities were found to be introduced from the crucible log.

Table 4.1   Composition of stainless steel (SST) assay.

Element name	Fe	Cr	Ni	C	Si	P	S	Mn	Mo
SST 304L(%)	67.935	19.0	10.0	≤0.03	≤1.0	≤0.035	≤0.03	≤2.0	-
SST 316L(%)	63.895	17	13.5	≤0.03	≤1.0	≤0.045	≤0.03	≤2.0	2.5

The major steps of the smelting process are briefly described as below[57]:

1. Cleaning the pot/crucible: put pure iron into the pot and maintain the pressure of vacuum chamber to a certain value and melt the pure iron into the liquid form. Then remove this liquid iron later to clean the surface;

2. Clean the Cr, Ni (for 304L), Mo (for 316L) and pure iron, and then put them into the pot and maintain the pressure of chamber to a certain value and then heat and melt the pure iron and raw materials together;

3. Keep pumping the pressure of the chamber to remove the H_2, N_2, and O_2 gas;

4. In the vacuum chamber, now mix liquid metal with the rest of the raw material into the pot;

5. Cast the mixture into an ingot shape;

6. Finally, open the chamber and take out the low level background SST ingot.

In so doing, no additional radioactive contamination was introduced in the custom-made 316L. We adopted the different assay methods (see the details in Sec. 4.2) to test a number of samples (see the details in Sec. 4.3),

1. The raw iron sample is used for testing the input material.
2. The ingot sample is used for testing the pot and pot cleaning process.
3. The custom-made 304L sample is used for testing the addition of Cr and Ni.
4. The custom-made 316L sample is used for the final product. Two commercial 304L and 316L samples are also tested for a comparison.

We found a significant difference between the custom-made and the commercial samples. We attributed this difference to the chemical composition and smelting process.

4.2   Assay methods

We have adopted two kinds of assay methods to investigate the contamination of our samples. The GDMS (Glow discharge mass spectrometer) is commercially known for spectrometry. This is the efficient method to investigate the concentration of any metal. The HPGe gamma ray spectroscopy is used for conventional sample investigations[58]. HPGe gamma spectroscopy is playing a vital role to measure the low level radioactive and environmental backgrounds[40,59,60]. Typically, the background of low level background HPGe detectors come from:

1. Cosmic radiations; including backgrounds directly from cosmic radiations and

indirectly from secondary radiations.

2. Environmental contamination, mainly form the natural radioisotopes, i.e. the ^{238}U and ^{232}Th chains, and the single radioisotope, ^{40}K, and some neutron sources will be consider as well, such as unstable fissions of neutron rich nuclides and (α, n) reactions;

3. Contamination in the detector and construction material[61–63].

To minimize background contaminations, we introduced passive, active and graded shields of different materials e.g. Cd, Cu, Pb, polythene and etc. and introducing anti-veto approach like anti-cosmic ray and anti-Compton systems[61,64,65]. It's always the best choice to install the HPGe spectrometer underground because cosmogenic backgrounds can be removed due to the rock overburden.

A HPGe facility was installed at ground level in Engineering Physics (Tsinghua University, Beijing) building in 2004. This facility was referred as to HPGe(THU) in this thesis. It has been used for various sample investigation.

Another low level gamma-ray germanium-spectrometer, was referred as to HPGe(CJPL) in this thesis, was installed at CJPL in 2012. Previously, this spectrometer was used for the China dark matter experiment (CDEX) detector[41].

4.2.1 GDMS

Glow Discharge Mass Spectrometer (GDMS) is commercially known for element spectroscopy. GDMS was established as an efficient and powerful analytical approach for tracing elements in test samples[66–69]. Some selected results are shown in Table 4.3.

4.2.2 HPGe at Ground level Tsinghua

A HPGe detector was installed at ground level in Engineering Physics (Tsinghua University, Beijing) building in 2004. It has been used for various sample investigation. The spectrometer is with low background against Compton scattering. The gamma spectrometer is made up of HPGe detectors and can also be used as NaI (Tl), NE110 plastic scintillation crystal ring cylinder anti-coincidence shield anti-coincidence detector. Lead, copper for shielding together with a paraffin screen cover. The whole spectrometer structure is shown in Figure 4.1 and detector layout in Figure 4.2[70]. In Figure 4.2, the schematic view of HPGe(THU), major parts of the detector are labeled with the different

colors. The tests at HPGe(THU). Six samples with the different grades of stainless steel the raw iron and ingot are shown in Figure 4.3.

Figure 4.1   HPGe(THU) detector layout. Where the top of the detector consists of one shielding material (including lead, paraffin and SST) and PMT's. The bottom of the detector is filled with the N_2 gas to suppress the environmental backgrounds.

4.2.3   HPGe at Underground (CJPL)

HPGe(CJPL) facility was fabricated by CANBERRA. The layout of HPGe(CJPL) is shown in Figure 4.4. The dimensions of HPGe crystal are, 59.9 mm in diameter and 59.8 mm in height. To suppress the background, a cryostat was built with ultra-low background aluminium. Due to high contamination, the preamplifier is placed outside the shielding. HPGe(CJPL) has a huge sample screening box with the dimensions of $30 \times 30 \times 63$ cm^3. HPGe(CJPL) used custom-made passive graded shielding, which offer low background. The inner shielding of the detector is made of oxygen free high purity copper, which is polished with a sand paper and cleaned with ethyl alcohol to make sure no external/surface contamination introduced. 3-layers of common ^{210}Pb has been introduced, each 5 cm thick, and are covered with the copper. Lead bricks were cleaned with ethyl alcohol before placed in shielding. The outermost borated polyethylene plate is used to shield the neutrons[71]. Figure 4.5 shows the comparison of six samples in HPGe(CJPL), including the raw iron sample, the ingot sample, the commercial 304L and 316L samples and, the custom-made 304L and 316L samples.
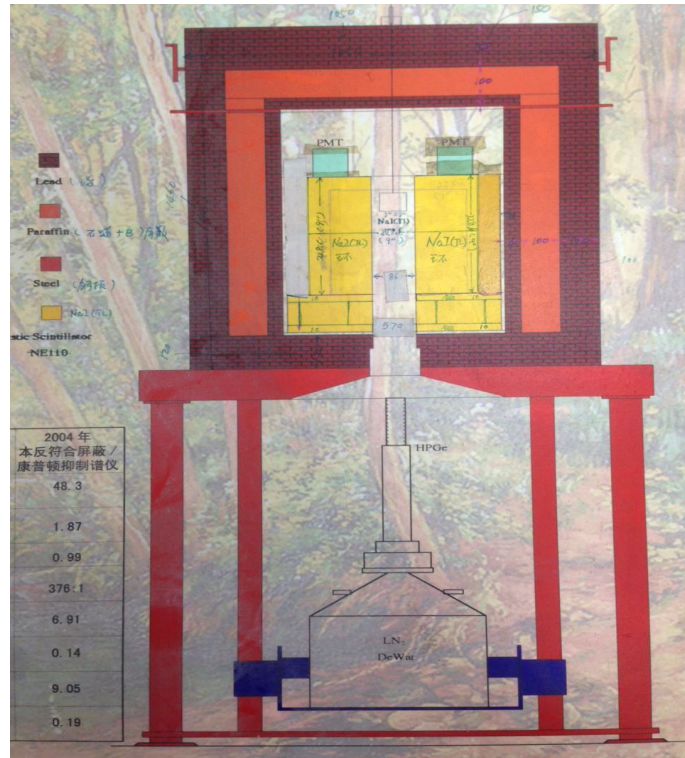
Figure 4.2   The schematic view of the HPGe(THU) detector. Different colors are used to illustrated, the different parts of the detector including the HPGe crystal and nitrogen gas (LN$_2$ DeWar) for flushing.
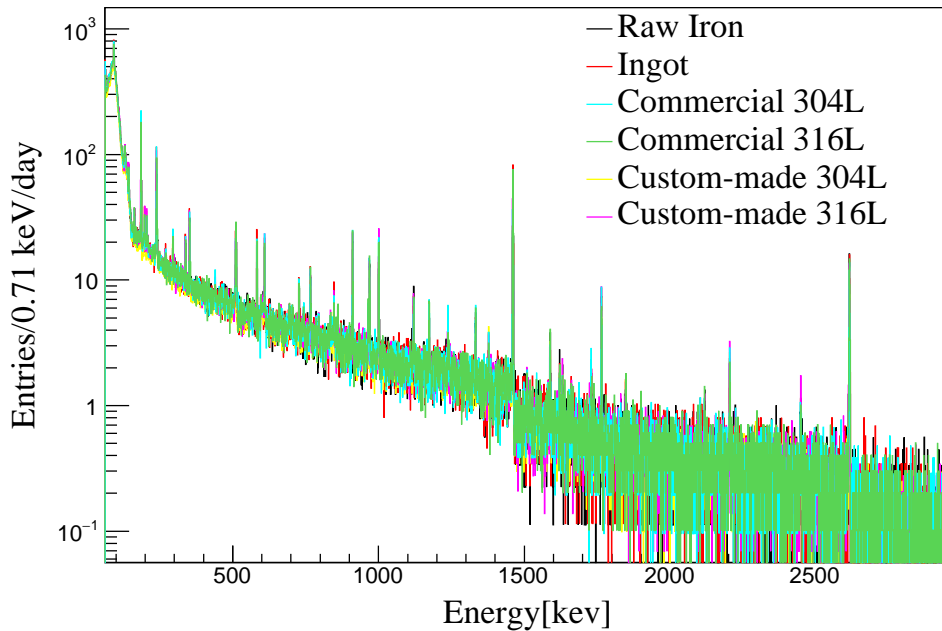
Figure 4.3   The tests of six samples in HPGe(THU).
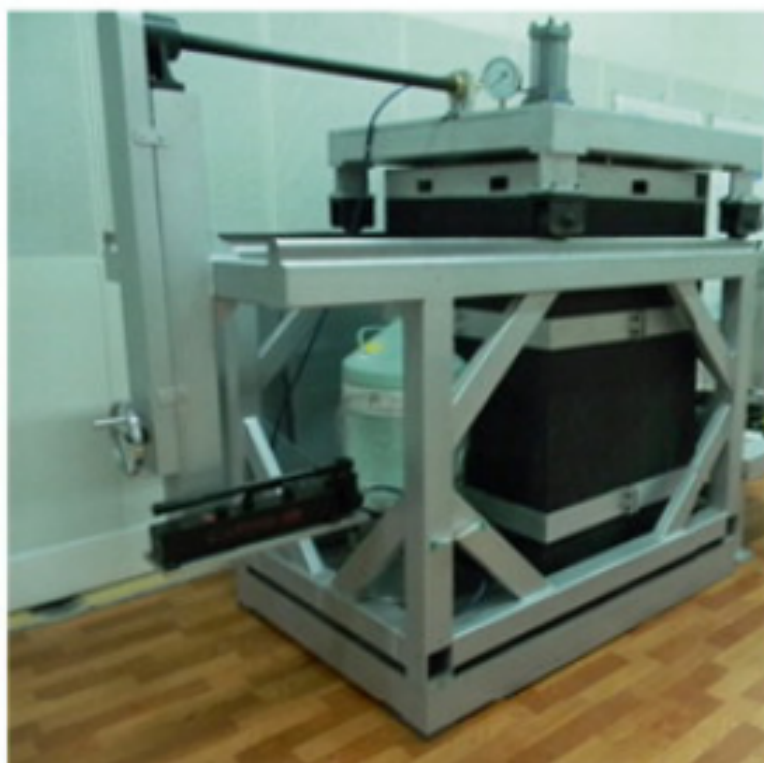
Figure 4.4   HPGe (CJPL) detector view.
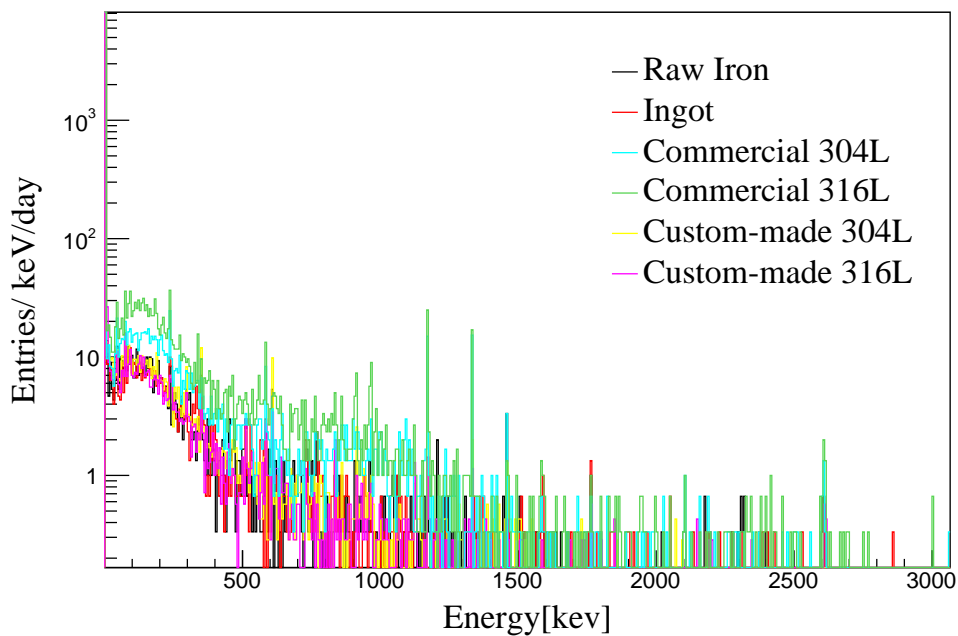
Figure 4.5   The comparison of six samples in HPGe(CJPL), including the raw iron sample, the ingot sample, the commercial 304L/316L samples and the custom-made SST304L/316L samples .

4.2.4   HPGe(THU) vs. HPGe(CJPL)

We compared the test results with the two HPGe detectors, at Tsinghua and CJPL Figure 4.6, shows that, the sensitivity at ground level detector is low, since there is the environmental contamination at the ground level and no overburden to the environmental radioactive background, however the ground level detector is more convenient for a initial screening for samples.
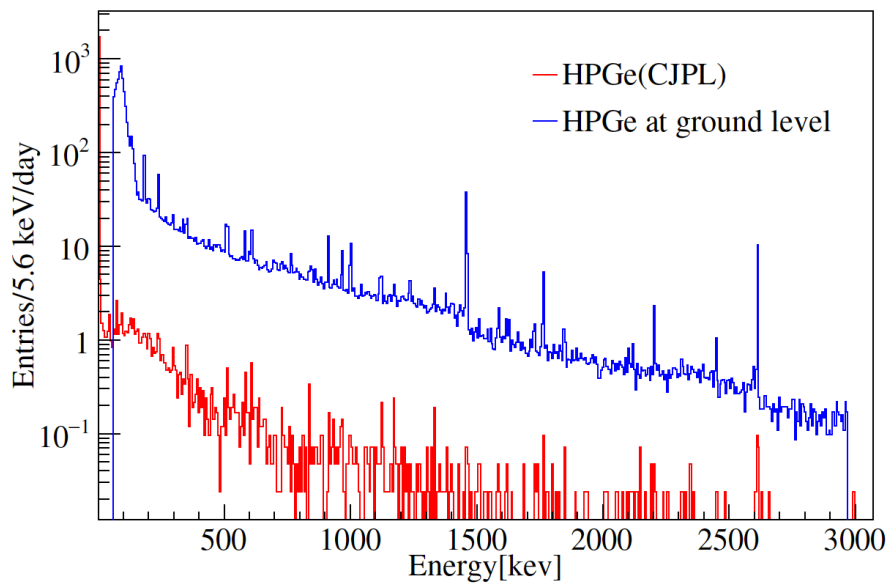
Figure 4.6   HPGe(CJPL) vs. HPGe(THU). The red spectrum is measured by HPGe(CJPL), while the blue spectrum is measured by HPGe(THU). The sensitivities for the two detectors are much different. The HPGe(THU) has a lower sensitivity than the HPGe(CJPL).

Table 4.2 gives the counting rates of different HPGe detectors at various labs. The background rate at CJPL is as low as 0.413 counts/min. We note that the rate at CJPL is higher than those at LNGS. This is understood to be due to an issue of the radon control, which is still needed to improve at CJPL.

4.2.5   Commercial 316L vs. custom-made 316L

Commercial 316L vs. Custom-made 316L samples, where commercial 316L is purchased from the market for comparison purposes. We made comparison with our custom-made 316L sample can be seen in Figure 4.7. Both spectra are measured by the HPGe(CJPL).

Table 4.2   The background rates of major HPGe counting facilities at various ground and underground labs.

Name	Laboratory	Overburden m.w.e	Energy range (keV)	Background rate (counts/min)
MELISSA[72]	KURF	1450	40 - 2700	5.42
CORRADO[72]	MPI-K	15	100 - 2700	3.20±0.01
Gator[72]	LNGS	3500	100 - 2700	0.157±0.001
GeMPI[72]	LNGS	3500	100 - 2740	0.0279±0.0004
HPGe(THU)	Tsinhua	0	60 - 2700	9.56
HPGe(CJPL)	CJPL	6720	40 - 2700	0.413
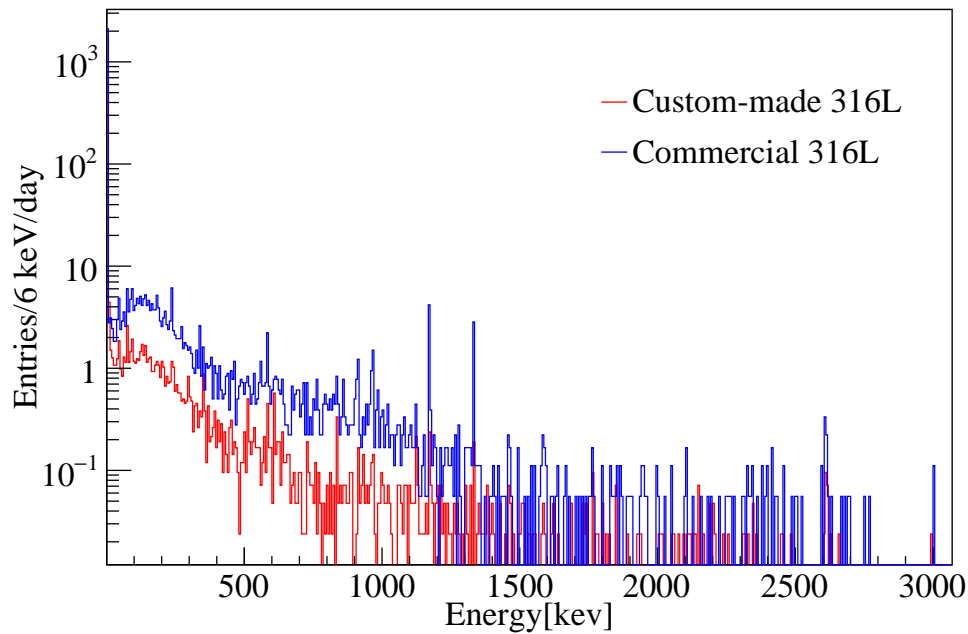
Figure 4.7   Test results of commercial 316L and custom-made 316L SST in HPGe(CJPL).

4.3   Assay results

We divided the assay results into three portions:

4.3.1   GDMS results

GDMS is a fast method to analyse the chemical composition of any solid and can measure the complete profile of solids. We tested five sample (raw iron, ingot, commercial 316L, custom-made 304L and 316L), the complete profile of selected samples can be seen in Figure 4.8. Where the radioactive concentration is in g/g. One can

conclude from Figure 4.8, that the commercial 316L sample have much more radioactive contamination than the custom-made 316L sample. Table 4.3 gives the chemical element analysis from GDMS for the two samples.
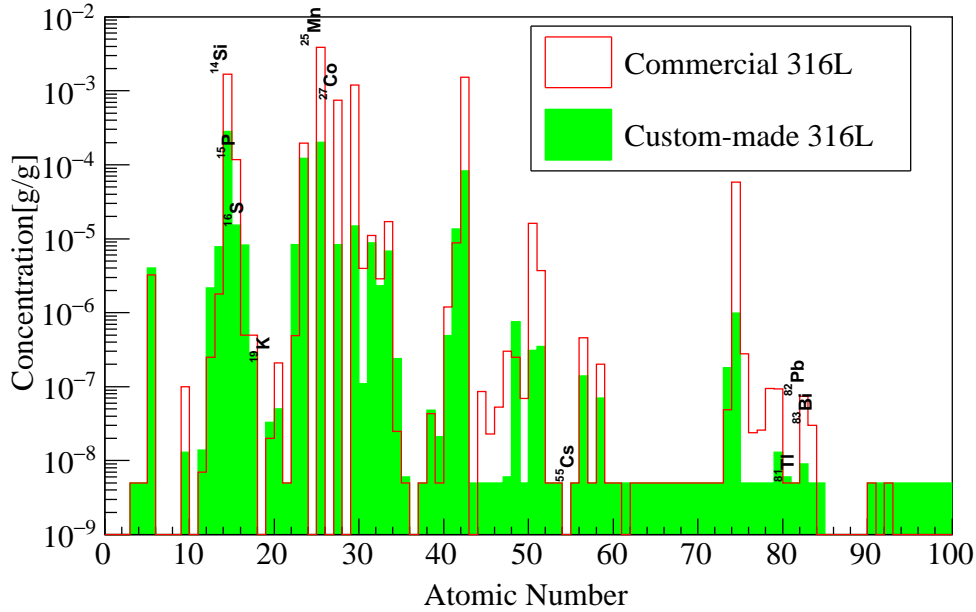
Figure 4.8　GDMS profile for selected samples including one customized SST samples.

4.3.2　HPGe results

4.3.2.1　Counting rates

Counting rates can be extracted from the Figure 4.5, and estimated by using a Gaussian fitting function as follows:

$$f(x; \mu, \sigma^2) = \frac{1}{\sqrt{2\pi\sigma^2}} \exp\left(\frac{-(x-\mu)^2}{2\sigma^2}\right), \tag{4-1}$$

where mean (μ) and resolution (σ^2) are two fitting parameters. Eq. (4-1) was used to fit the signal peak, while the first order polynomial function was used for fitting the background. An example of fitting result is illustrated in Figure 4.9.

4.3.2.2　Geant4 simulation for HPGe(CJPL)

Currently, it is very common to use Geant4 Monte Carlo simulation to validate the measurements. In this thesis, we used Geant4 to simulate HPGe(CJPL). The geometrical setup of HPGe(CJPL) is shown in Figure 4.10. The major dimensions of HPGe(CJPL)

Table 4.3   These results are measured by the commercially known GDMS facility. Comparison of different gamma peaks in the two samples of commercial 316L and custom-made 316L for detector construction of Jinping underground neutrino experiment. Each sample consists of different nuclides. The results are given in g/g.

Nuclide	Commercial 316L $\times 10^{-6}$ g/g	Custom-made 316L $\times 10^{-6}$ g/g
Pb	0.074	0.009
Bi	0.03	<0.005
Tl	<0.005	<0.005
K	0.02	0.033
Co	742	8.39
Cs	<0.005	<0.005
Si	1671	284
Mn	3853	202
P	118	15.4
S	<0.5	8.25
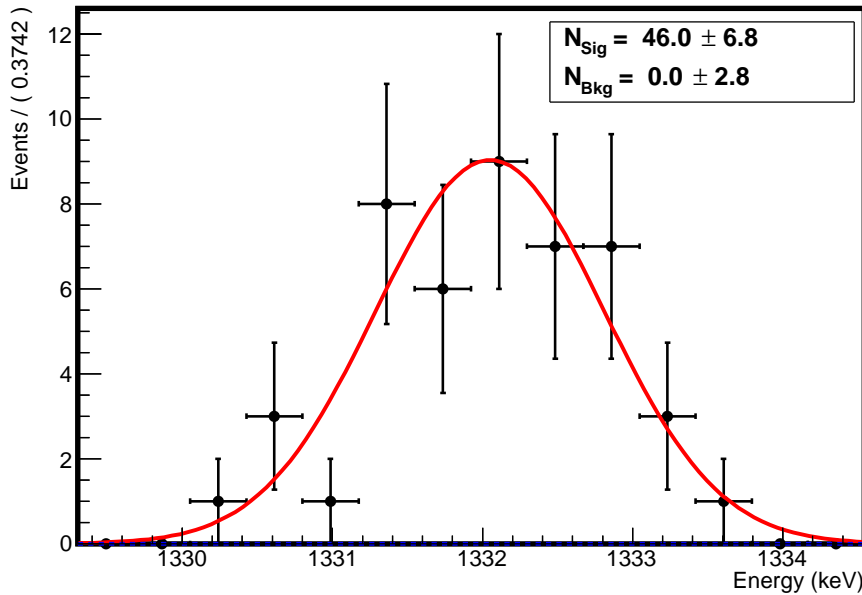
Figure 4.9   The example of fitting to the ^{60}Co signal peak in the data for the commercial 304L sample.

are given in the Sec. 4.2.3. These dimensions are used in the simulation. The HPGe detector is placed inside and covered by the shielding.
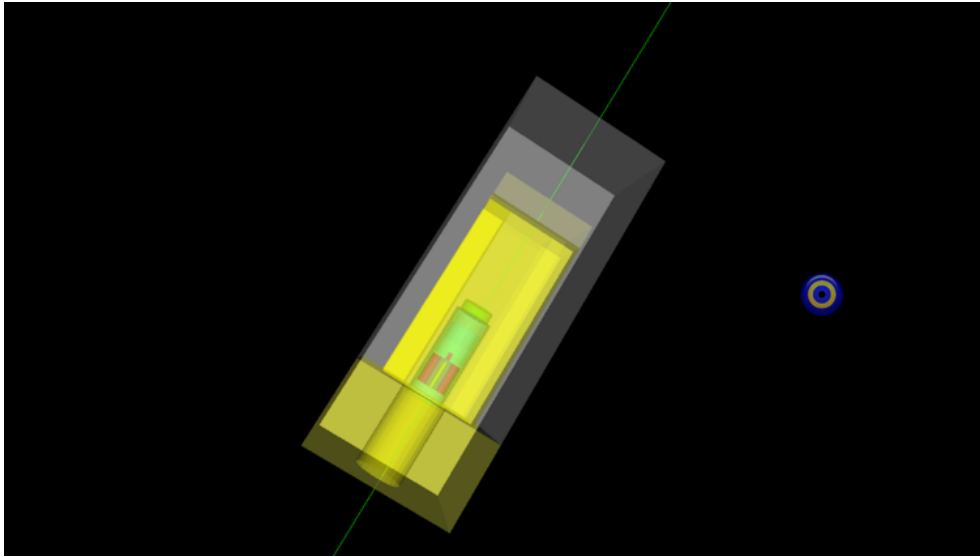
Figure 4.10   The schematic view of Geant4 simulation for HPGe(CJPL).

4.3.2.3 Efficiency evaluation for HPGe(CJPL)

A Geant4 simulation is used to estimate the efficiency of HPGe(CJPL). To validate the efficiency of the detector, we used the SST sample in the simulation. The gamma efficiencies are shown in Figure 4.11.
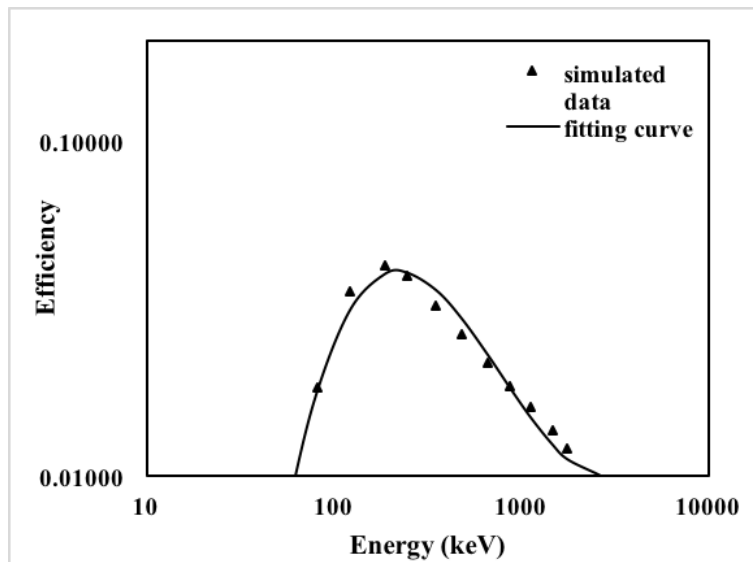
Figure 4.11   HPGe(CJPL) efficiency estimated by Geant4. The efficiency is observed as a function of energy and solid curve indicates the fitting results, with the fitting function given in Ref. [71].

4.3.2.4 Radioactivity contamination

In this thesis, all the results are reported with nitrogen flushing. The background spectra can be seen in the Figure 4.5. The histogram in blue is commercial 316L and the histogram in red is custom-made 316L. Both spectrums measured by HPGe(CJPL) will be used for further usage in low-energy neutrino experiments.

Radioactivity concentration for the selected radioisotopes is estimated with Eq. (4-2)[73]:

$$A = \frac{N_{net}}{\varepsilon t \gamma m}. \qquad (4\text{-}2)$$

Where A indicates the radioactivity contamination in Bq/kg, N_{net} represents the net counts, ε represents the efficiency, t is the data taking time, γ represents the branching ratio and m is the sample's mass. The detailed results can be seen in Table 4.5.

All the four spectra are presented in Figure 4.12 are measured by HPGe(CJPL) detector. In Figure 4.12, we give the comparison among the four SST samples, in which commercial 304L and commercial 316L samples were purchased from the market, while custom-made 304L and 316L are the customized samples. By comparing these fours samples, one can conclude that the samples from the market have much more contamination. The contamination rates of these samples, corresponding to each isotopes/nuclide or single peak value are listed in Table 4.5.

4.3.3 GDMS vs. HPGe results

We compared the GDMS results with HPGe and found that GDMS is the fastest way to know the contamination of a sample, but the sensitivity is not better than that with HPGe(CJPL).

Table 4.4   Calculated conversion factors for different chain/nuclide. The conversion factors further used in our final contamination measurements in Tab. 4.6.

Isotope/Nuclide	Half life	Atomic mass	Conversion factor
^{238}U	4.468×10^9 years	238.05	1ppb = 12.4 mBq/Kg
^{232}Th	1.405×10^{10} years	232.03	1ppb = 4.06 mBq/Kg
^{40}K	1.277×10^9 years	39.96	1ppb = 259.4 mBq/Kg
^{60}Co	5.2714 years	59.93	1ppb = 4.19×10^{10} mBq/Kg

Table 4.5   Comparison of different gamma peaks in the six samples, SST sample for detector construction of Jinping underground neutrino experiment. Radioactive contamination rate in Bq/kg. Where symbol < indicates the upper limit for background @ 95.% CL.

Decay Chain	Isotopes	Peak keV	Raw Iron Bq/kg	Ingot Bq/kg	CustomMade 304L Bq/kg	CustomMade 316L Bq/kg	Commercial 304L Bq/kg	Commercial 316L Bq/kg
U-238	Ra-226	186.21	< 0.0525	< 0.0540	< 0.0383	< 0.0365	< 0.0830	0.1019 ± 0.02775
	Pb-214	295.21	0.0112±0.0025	< 0.0082	0.0116 ± 0.0021	< 0.0105	< 0.0153	< 0.0142
	Pb-214	351.92	0.0057±0.0016	< 0.0048	0.0132 ± 0.0013	< 0.0056	< 0.0056	< 0.0093
	Bi-214	609.31	0.0058±0.0015	< 0.0063	0.0145 ± 0.0014	< 0.0054	< 0.0047	< 0.0071
	Bi-214	1764.5	< 0.0172	< 0.0216	< 0.0059	< 0.0106	< 0.016	< 0.0179
	Bi-214	1120.3	< 0.0033	< 0.0031	< 0.0145	< 0.0176	0.0110±0.0041	< 0.0227
Th-232	Ac-228	209.25	< 0.0491	< 0.0635	< 0.0304	< 0.0476	<0.0555	0.0690 ± 0.0214
	Ac-228	338.92	< 0.0148	< 0.0161	< 0.0079	< 0.131	<0.0081	<0.0247
	Ac-228	911.20	< 0.0106	< 0.0074	0.0059±0.0017	< 0.0048	< 0.0144	0.0348 ± 0.0051
	Ac-228	968.97	< 0.0101	< 0.0114	< 0.0075	< 0.0067	< 0.0190	< 0.0259
	Tl-208	583.14	< 0.0038	< 0.0038	< 0.0014	< 0.0020	0.0054±0.0010	0.0099±0.0012
	Tl-208	2614.7	< 0.0051	< 0.0048	< 0.0018	< 0.0023	< 0.0047	< 0.0062
K-40	K-40	1460.82	< 0.4637	< 0.2803	0.0138±0.0048	< 0.0129	0.3600±0.0927	< 0.3553
Co-60	Co-60	1173.23	< 0.0024	< 0.0016	0.0013±0.00035	0.0014±0.0004	0.0150±0.0017	0.0354±0.0046
		1332.49	< 0.0024	< 0.0027	< 0.0029	< 0.0017	0.0238±0.0018	0.0283±0.0032
Cs-137	Cs-137	661.66	< 0.0017	< 0.0017	< 0.0012	< 0.0011	< 0.0025	< 0.0023
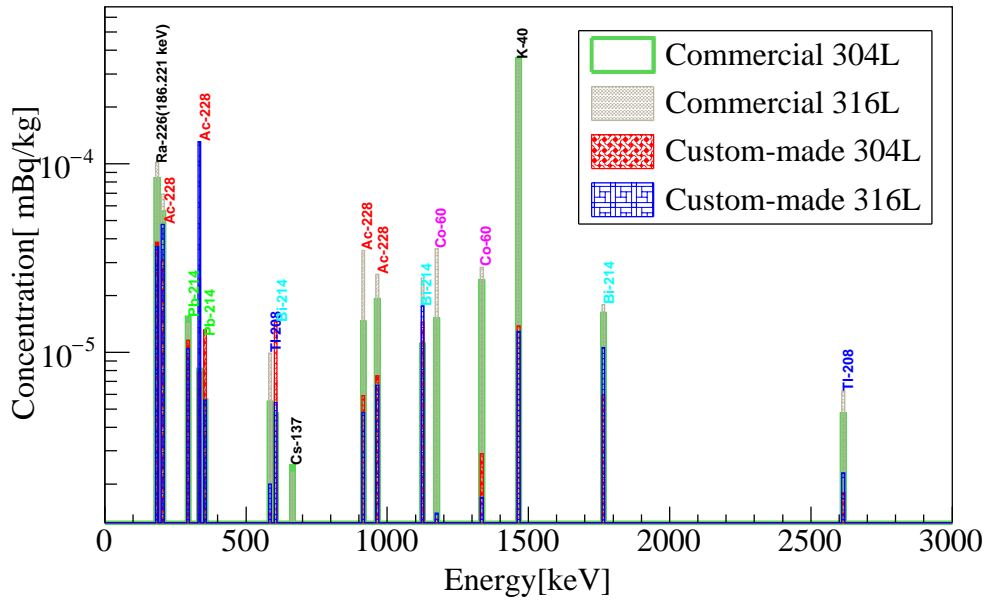
Figure 4.12   HPGe(CJPL) profile of the four SST samples, in which the commercial 304L and commercial 316L samples were purchased from the market, while the custom-made 304L and 316L were produced with a special procedure. By comparing these fours samples, one can conclude that the commercial samples have more contamination.

4.4   Discussion

Stainless steel is an important material in today's detector construction, and it will be used for the neutrino detector construction at CJPL. Thus it is important to investigate the radioactive contamination and to ensure that no unwanted contaminations are found. The commercial 316L(0.52381 kg) and custom-made 316L (0.56427 kg) samples were measured using the HPGe(CJPL) detector. GDMS facility provides the complete profiles of the sample's elements composition. But our main intentions are only few radioactive nuclides. In Table 4.3 selected results can be seen. The custom-made 316L by smelting process is chosen.

The detailed results of HPGe(CJPL) are shown in Table 4.5 with the six samples, comparison of different gamma peaks in the six samples. Radioactive contamination rate in Bq/kg. The radioactivity is estimated by using the Eq. (4-2).

Some important peaks are for 351.92 keV ^{238}U/^{214}Pb, for 583.14 keV ^{232}Th/^{208}Tl and for 1460 keV ^{40}K . These peaks are very sensitive to the solar neutrino measurement window and contamination rates including few main peaks are presented in Table 4.5. The major contamination is from ^{222}Rn induced and some are from the detector shielding.

When ^{238}U and ^{232}Th are in the secular equilibrium, most of the contamination results are given in the upper limit. So we assign the background for the whole chain, to select the best value among all the number. We calculated the contamination rates in the SST, especially in the custom-made 316L sample, which will be used in the future neutrino experiments at CJPL.

Table 4.6 gives a summary of background estimation, which has been measured by two different facilities HPGe(CJPL) and GDMS. The contaminations in rock have been reported in Ref.[16]. HPGe(CJPL) has the lowest rock contamination than the other experiments. In Table 4.6, we made a comparison with some experiments[40], and found that the level of radioactivity of the sample, especially due to ^{232}Th and ^{40}K, reached to the required one.

4.5 Summary

We investigated the whole smelting procedure to produce the low level background SST. We adopted different assay methods to investigate the contaminations in our samples. We used professional facilities like GDMS to measure the radioactivity in our samples.

A low background HPGe(CJPL) facility, was installed at CJPL and used for various detector's material testing, including to investigate materials for Jinping neutrino experiment, which is very sensitive to the rare event and also for the environmental monitoring. We have reported our comparison with other experiments with respect to the radioactivity in SST.

Table 4.6   Background comparison with different units among the iron steel samples to be used at Jinping.

Radioisotopes	Custom-made 316L			304L		S-275	
	HPGe(CJPL)	GDMS		Borexino[40]		Next IBD[74]	
	mBq/kg	mBq/kg	g/g	mBq/kg	g/g	mBq/kg	g/g
^{238}U	< 5.4	<61.75	$< 5 \times 10^{-9}$	4.56	3.7×10^{-10}	32	2.6×10^{-9}
^{232}Th	< 2.0	<20.3	$< 5 \times 10^{-9}$	11.368	2.8×10^{-9}	1.9	1.16×10^{-9}
^{40}K	< 12.9	1.023	33×10^{-9}	<14	$< 4.5 \times 10^{-7}$	3.2	1.03×10^{-7}
^{60}Co	1.4±0.4		8.39×10^{-6}		6.0		1.8

Chapter 5   Study of Geo-neutrino at Jinping

5.1   Introduction

The production of heat in the Earth is influenced by radioactive elements releasing heat when decaying to more stable nuclei. These decays are mainly by ^{232}Th, ^{238}U and ^{40}K decays series. Without much information about the levels of these elements it is not easy to differentiate the heat originating from radiative decays and the primordial heat remnant from the initial gravitational collapse. An approach to estimate the radioactive isotopes present within the Earth is to measure the flux of v's produced in the decay series of ^{232}Th and ^{238}U.

5.2   Geophysical heat budget

The present estimates of the total heat radiated from the Earth, including those from the oceanic and continental crust, is 31 ± 1 terrawatt (TW) by H.N.Pollack et al.[75]and A.M. Hofmeister[76]. The estimate was derived from 24,744 bore-hole observations at 20,201 points, covering about ~60%of the Earth with a resolution of $5° \times 5°$. Most of the heat is radiogenic with a small ratio coming from chemical contribution and primordial heat. The sources of heat vary for the region of the Earth and depend on the composition and the levels of convection and conduction for the region. As shown in Figure 5.1, the different density layers of the Earth, except the liquid outer core and upper mantle, which contain partial melts, are solids. Due to different layering of the Earth as shown in Table 5.1, the solid layers release heat slowly and are affected by the conduction. On the other hand, the liquid layers can transfer heat through convection at a faster rate. The layering of the Earth was due to the Earth's formation and gravitational compression.

5.2.1   Tertiary planet formation

During star formation, a rotating cloud of interstellar dust and gas collapses gravitationally towards its center of mass. This gas is made particularly of hydrogen (H) and helium (He), with a small ratio of heavier elements deposited by extremely high
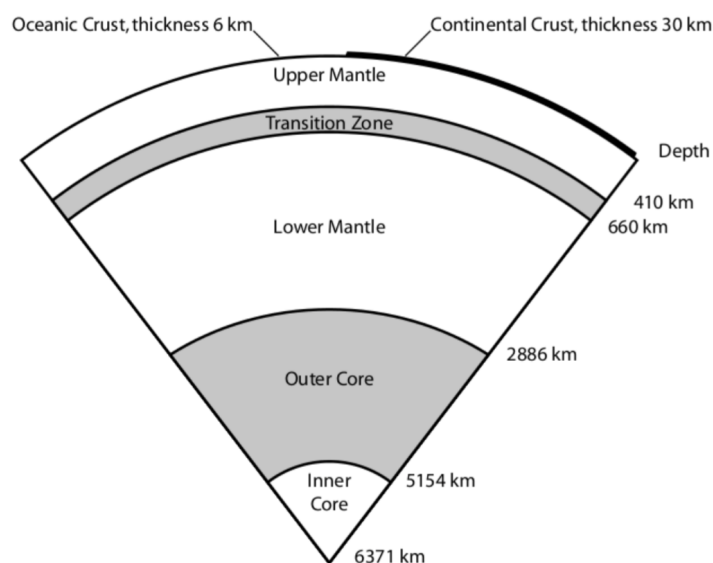
Figure 5.1   Radial distribution of Earth's interior[77].

Table 5.1   Radial distribution of the Earth's interior with regional mass distributions[77].

Zone	Depth [km]	Mass [10^{21}kg]	Mass Fraction [%]	Average Density [kgm^{-3}]
Oceanic crust	0~6	6	0.1	3,100
Continental crust	0~30	19	0.3	2,700
Upper mantle	(6,30)-410	615	10.3	3,350
Transition zone	410~660	415	7.0	3,860
Lower mantle	660~2886	2,995	49.6	4,870
Outer core	2,886-5,140	1,867	31.1	11,000
Inner core	5,140-6,371	5,975	100	5,515
Whole Earth	0-6,371	5,975	100	5,515

energetic stellar events such as supernovas. When particles collide into each other most of the energy of the gas is convert into heat or thermal energy. A large portion of this matter gathers at the center, making a large mass of dense, hot matter which will finally create hydrogen (H) fusion thus forming a star[78–80].

5.2.2   Geochemical Earth model

The geochemical phases of the Earth occurred through slow cooling (as shown in Figure 5.2), which happened during the early stages of our planets formation and shaped how the materials within our planet are arranged. The measurement of neutrinos can help

us to know the composition of the Earth, through direct measurement.

5.2.3 Bulk silicate Earth (BSE) model

It is difficult to understand the Earth's chemical composition, but there are several estimates on the chemical composition of the earth made by carbonaceous and iron meteorites group. These are named after the Ivuna meteorite and very close to that of solar photosphere. By understanding the chondrite composition and considering geological and lithological estimations, the BSE model gives acceptable measurements of the Earth's composition[81]. The Earth model provides a theoretical rock composition, which guides us to to know about the mantle's composition, before and after the separation, mantle to crust. In accordance with these models, the original mantle would have ^{238}U and ^{232}Th in amounts as high as 17.3 ± 3 ppb (part per billion) and 63 ± 10 ppb respectively[82].

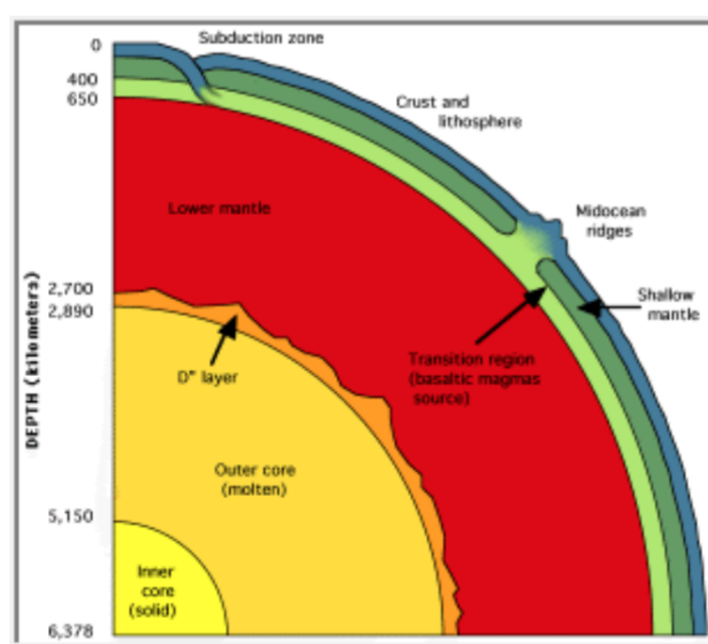Figure 5.2   Geochemical density distribution.

5.2.4 Core

Seismic waves can be used to know the Earth's core and it behaviour. The chemical behaviour of the Earth's core can be understood by the analysis of meteorites, particularly carbonaceous and iron meteorites. The Earth's chemical composition can be estimated by subtracting silicate from carbonaceous chondrite composition. It is also believed that

refractory lithophile elements like ^{238}U and ^{232}Th are not present in the core, despite the Earth's models; a core made by low atomic elements like hydrogen, carbon, nitrogen, magnesium, silicon and sulphur can be contained in such high density alloys[82].

5.2.5   Mantle

Continental crust (CC) is formed due the melting of mantle.   In this process, numerous elements are formed such as ^{238}U and ^{232}Th from mantle to crust.   This melting occurs at a 30 ~ 70 km and heat convection happens inside the mantle, which creates depletion and form a incompatible elements in the Earth. We only know the tiny information of lower mantle part, it impossible to reach that part. It is easier to understand the upper part of the mantle[83], numerous samples of ultramafic massifs are available.

5.2.6   Oceanic crust and sediment

The composition of CC in the Earth not more than 0.4%.   It is believed that uranium (as shown in Table 5.2) and thorium (as shown in Table 5.3) only half of the continental crust.   CC is not as dense as the oceanic crust.   The oceanic crust is homogeneous on average and more dense than CC. By knowing the composition of the oceanic crust is basaltic with the ^{238}U and ^{232}Th concentration at ~ 0.10 ppm and ~ 0.22 ppm respectively[84].   The top layer of oceanic crust is sediment, which belongs to the volcanic and continental activity besides biological products. Geochemical samples can be collected through Deep Sea Drilling Project (DSDP), which estimates the ^{238}U and ^{232}Th concentration in the sediment to be 1.68 ppm and 6.91 ppm respectively[85].

5.2.7   Sources of terrestrial heat

A new planet has a sufficient amount of heat held within it from it's first gravitational collapse. Over time this heat is transported from its warm centre to the solid oceanic and

Table 5.2 ^{238}U Concentration in the continental crust.

| Name | Uranium Concentration [ppm] | | | |
	Upper crust	Middle Crust	Lower Crust	Average
Rudnick (1995)	2.8	1.6	0.2	1.42
McLenan (1999)	2.8	0.28	0.28	0.91
Wedepohi(1995)	2.5	0.93	0.93	1.7

Table 5.3 ^{232}Th Concentration in the continental crust.

| Name | Thorium Concentration [ppm] | | | |
	Upper crust	Middle Crust	Lower Crust	Average
Rudnick (1995)	10.7	6.1	1.2	5.6
McLenan (1999)	10.7	1.06	1.06	3.5
Wedepohi(1995)	10.3	6.6	6.6	8.5

Table 5.4   Summary of ^{238}U and ^{232}Th concentration in each region.

Region		Uranium [ppm]	Thorium [ppm]	Reference
Sediment	Continental	2.8	10.7	Plank et al.
	Oceanic	1.68	6.91	Plank et al.
Continental crust	Upper	2.8	10.7	Rudnick et al.
	Middle	1.6	6.1	Rudnick et al.
Oceanic crust	-	0.1	0.22	Taylor et al.
Mantle	Upper	0.012	0.048	-
	Lower	0.012	0.048	-
Core	Outer	0	0	McDonough
	Inner	0	0	McDonough
Bulk Silicate	-	0.02	0.08	McDonough

continental crusts. The heat finally escapes through radiation. The cooling is slower because of inner heat production within the core, mantle, and crust, which coming from many possible sources, with a large emphasis on radioactive decay energy. In order to measure the level of heat generation inside the Earth, it is essential to correctly measure the level of different heat sources inside the Earth and set constraints on the amount of recent formed heat which resembles with the heat transfer inside the Earth. The disappearance of the total heat on the Earth's surface, as described earlier, is 31 ± 1 TW[76]. This heat falls into two types, primordial heat and new heat. Primordial heat is any form of heat which originated from the energy of the initial gravitational collapse of the hot protoplanet materials. This heat is not enough responsible to warm our planet, thus there are also other factors such as new heat is produced by chemical reactions and from radioactive decays[83].

5.3 BSE model for Jinping

A $1° \times 1°$ topological map of the density $\rho(\vec{r})$ in the Earth crust is used in Eqs. (5-6) and (5-7), and was obtained from CRUST1.0. The assumption employed for the mantle is from Huang *et al*[86]. For the computation of flux, a $1° \times 1°$ tile is further divided into subtiles to obtain the propagation distance L. The abundance of HPEs $A_i(\vec{r})$ in geological layers and the intrinsic radioactive element properties. The abundance is assumed to be uniform in every layer. The energy spectra of HPEs are obtained as in Sec. 5.4.

5.4 Energy spectra of geoneutrinos

Radioisotopes that are found in the Earth's interior are fall into three major kinds; isotopes in the ^{232}Th ($\tau_{\frac{1}{2}} = 14.0 \times 10^9$ year) decay chain, isotopes in the ^{238}U ($\tau_{\frac{1}{2}} = 4.47 \times 10^9$ year) decay chain, and ^{40}K ($\tau_{\frac{1}{2}} = 1.28 \times 10^9$ year). Besides that, there are also minor isotopes decays in the Earth, which have a much shorter half life time, e.g ^{237}Np($\tau_{\frac{1}{2}} = 2.0 \times 10^6$year). They can be ignorable due to their low abundances and very

small Q values (e.g. ^{138}La, ^{87}Rb and etc.)[83]. The reactions are follows:

$$^{238}\text{U} \rightarrow ^{206}\text{Pb} + 8\alpha + 6e^- + 6\bar{\nu}_e + 51.698 \text{ MeV},$$

$$^{232}\text{Th} \rightarrow ^{207}\text{Pb} + 7\alpha + 4e^- + 4\bar{\nu}_e + 46.402 \text{ MeV},$$

$$^{235}\text{U} \rightarrow ^{208}\text{Pb} + 6\alpha + 4e^- + 4\bar{\nu}_e + 42.652 \text{ MeV}, \tag{5-1}$$

$$^{40}\text{K} \rightarrow ^{40}\text{Ca} + e^- + 4\bar{\nu}_e + 1.311 \text{ MeV} \quad (89.3\%),$$

$$^{40}\text{K} + e^- \rightarrow ^{40}\text{Ar} + \nu_e + 1.505 \text{ MeV} \quad (10.7\%).$$
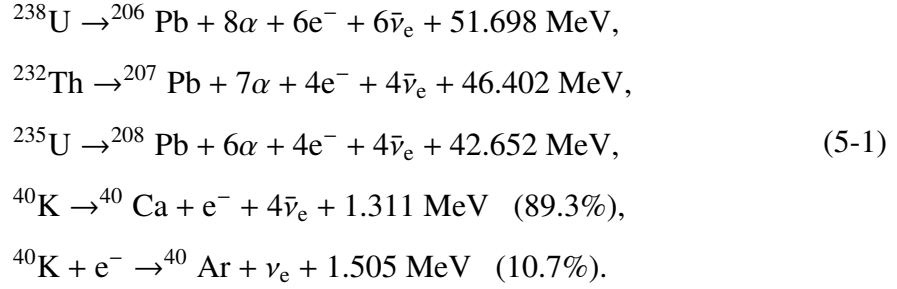
Except for the K-shell EC of ^{40}K, all the other β decays produce $\bar{\nu}_e$'s, comprising the geoneutrinos. It is noted that only those from ^{232}Th and ^{238}U decay chains with energy above IBD threshold of 1.8 MeV can be detected.

In the estimation of the overall antineutrino intensity energy spectrum of each decay series, the shapes and rates of all single decays have to be incorporated: comprehensive calculations are needed to take into account 82 individual branches in ^{238}U and 70 individual branches in ^{232}Th. The only contributions to the geoneutrino signal detectable via IBD are from ^{214}Bi and ^{234}Pa in the ^{238}U series and ^{212}Bi and ^{228}Ac in the ^{232}Th series[87].
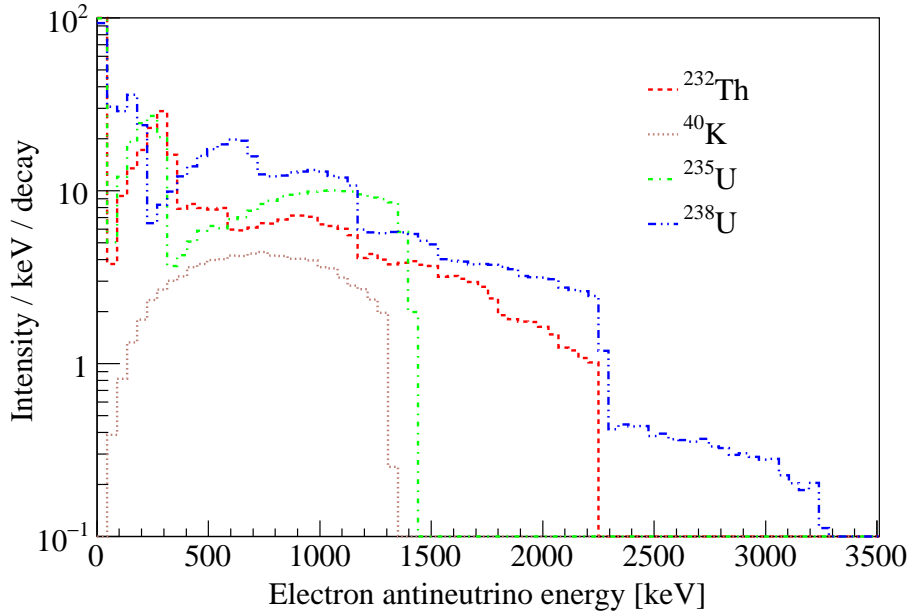

Figure 5.3   Geoneutrino energy spectra of U-series, Th-series and K.

It is noted that there is a few percent difference around 1 MeV for ^{238}U between the present Geant4 and S. Enomoto's calculation[88]. Both the ^{235}U and ^{40}K geoneutrinos are

below the IBD threshold of 1.8 MeV, as shown in Fig. 5.3, and cannot be detected via the IBD method.

Table 5.5   Radiogenic heat emission per decay, corresponding to isotopes/nuclide[88].

	^{238}U	^{232}Th	^{40}K $[\beta^-(89.28\%)]$	^{40}K [EC(10.72%)]
Q [MeV/decay]	51.7	42.7	1.311	1.505
Q_ν [MeV/decay]	3.96	2.23	0.724	0.044
Q_{heat} [MeV/decay]	47.7	40.4	0.587	1.461

Radiogenic heat emission can be calculated by subtracting Q [MeV/decay] from the Q_ν, Equation (5-2). The $\frac{dN}{dE}$ is neutrino intensity spectrum followed by Chapter 2.

$$Q_{heat} = Q - Q_\nu = Q - \int_0^{E_{max}} E_\nu \frac{dN}{dE} dE_\nu. \tag{5-2}$$

By adding, all the decays from individual branches from U, Th and K, the total radiogenic heat energy is shown in Table 5.5.

Table 5.6   Neutrino luminosity and emission of radiogenic heat[88].

	^{238}U	^{232}Th	^{40}K
Natural Abundance [%]	99.27	100	0.01167
N_{atom}/mass[1/kg]	2.530×10^{24}	2.596×10^{24}	1.506×10^{25}
Lifetime[sec]	2.034×10^{17}	6.397×10^{17}	5.814×10^{16}
N_{decay}/mass[1/sec/kg]	1.244×10^7	4.058×10^6	2.590×10^8
$N_{\bar{\nu}_e}/N_{decay}$	6	4	0.8927
$L_{\bar{\nu}_e}$ /mass[1/sec/kg]	7.464×10^7	1.623×10^7	2.312×10^8
Q_{heat} /mass[W/kg]	9.515×10^{-5}	2.628×10^{-5}	2.824×10^{-5}

Neutrino luminosity $L_{\bar{\nu}_e}$ is calculated by[83] as follows:

$$\text{Uranium} : \frac{L_{\bar{\nu}_e}}{\text{mass}} = 7.410 \times 10^7 \ [\bar{\nu}_e/\text{sec/kg}]. \tag{5-3}$$

$$\text{Thorium} : \frac{L_{\bar{\nu}_e}}{\text{mass}} = 1.62 \times 10^7 \ [\bar{\nu}_e/\text{sec/kg}]. \tag{5-4}$$

$$\text{Potassium : } \frac{L_{\bar{\nu}_e}}{\text{mass}} = 2.70 \times 10^4 \ [\bar{\nu}_e/\text{sec/kg}]. \tag{5-5}$$

5.5   Calculation of geoneutrino flux

The geoneutrino flux $\phi(E)$ can be estimated by the heat producing elements (^{238}U ,^{232}Th, and ^{40}K) at Jinping experiment site by integrating the grid-calculated geo-$\bar{\nu}_e$'s in the Earth propagating to Jinping site with an oscillation,

$$\phi_i(E)dE = \frac{X_i \lambda_i N_A}{\mu_i} n_\nu(i) \times \int \frac{A_i(\vec{r})\rho(\vec{r})}{4\pi L^2} P_{ee}^i(E,L) f_i(E) d\vec{r} dE, \tag{5-6}$$

where X indicates the natural isotopic fraction of radioisotopes/nuclide i (^{238}U ,^{232}Th, and ^{40}K), λ is representing decay constant corresponding to each i, N_A is Avogadro's number, μ is the atomic mass of i, n_ν is representing the number of antineutrinos emitted per decay of i; $A(\vec{r})$ is abundance of element for each i; $\rho(\vec{r})$ is density, L indicates the linear path to the Jinping detector; P_{ee} is the $\bar{\nu}_e$ survival probability and $f(E)$ is the normalized $\bar{\nu}_e$ energy spectrum of i.

Total geoneutrino flux ϕ_i from HPE i can be obtained by integrating the below Equation,

$$\begin{aligned} \phi_i &= \int \phi_i(E)dE \\ &= \frac{X_i \lambda_i N_A}{\mu_i} n_\nu(i) \langle P_{ee}^i \rangle \int \frac{A_i(\vec{r})\rho(\vec{r})}{4\pi L^2} d\vec{r}, \end{aligned} \tag{5-7}$$

where $\langle P_{ee}^i \rangle$ is the survival probability of $\bar{\nu}_e$. Except the vacuum oscillation effect, the three-generation Mikheyev-Smirnov-Wolfenstein (MSW) oscillation effect is also considered.

5.6   Backgrounds for geoneutrino signal

Borexino and KamLAND experiments have already studied that the backgrounds for geoneutrino signal are from the reactor neutrinos and non-neutrino backgrounds.

5.6.1   Reactor antineutrino backgrounds

Reactor antineutrino background (RAB) is the severe background for geoneutrino signal. RAB is the major man made source of antineutrinos and can not be reduced by

material purification or placing the detector in deep underground. The flux obeys the law of inverse distance square.

5.6.1.1 Differential neutrino flux of a single reactor

The major man-made source of antineutrinos is produced in the fission process inside the reactor core. The fissions of ^{235}U, ^{238}U, ^{239}Pu and ^{241}Pu provide the major source of energy in the nuclear reactors. The differential flux of antineutrino from the single reactor core can be estimated as

$$\phi(E_v) = \frac{W_{th}}{\sum_i f_i e_i} \sum_i f_i S_i(E_v), \tag{5-8}$$

where $\phi(E_v)$ represents the flux of antineutrinos, i represents the total number of isotopes, W_{th} represents thermal power of a reactor[89], f_i, represent the fission fraction of each isotopes, e_i represents the average energy released per fission of each isotope. A typical set of fission fractions, f_i, and the average energy released per fission, e_i, are followed in Table 5.7 and shown in Figure 5.4.

Table 5.7   Fission fraction and average released energy of each isotope.

Isotope	f_i	e_i [MeV/fission]
^{235}U	0.58	202.36 ± 0.26
^{238}U	0.07	205.99 ± 0.52
^{239}Pu	0.30	211.12 ± 0.34
^{241}Pu	0.05	214.26 ± 0.33

5.6.1.2 Total differential reactor neutrino flux

The total reactor neutrino background can be measured at Jinping, $\phi_{Jinping}$, thermal powers data of planned or currently running reactors can be used from IAEA[89], and the $\bar{v}_e$ survival probability is also used. $\phi_{Jinping}(E_v)$ can be shown:

$$\phi_{Jinping}(E_v) = \sum_i^{Reactors} \phi_i(E_v) P_{\bar{v}_e \to \bar{v}_e}(E_v, L) \frac{1}{4\pi L^2}, \tag{5-9}$$

$$P_{\bar{v}_e \to \bar{v}_e}(E_v, L) \approx 1 - \sin^2 2\theta_{12} \sin^2(1.267 \frac{\Delta M_{21}^2(eV)L(km)}{E_v(GeV)}), \tag{5-10}$$
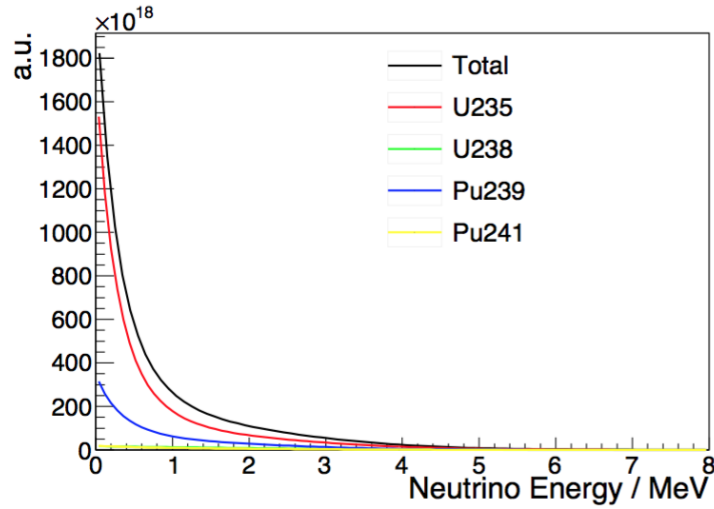
Figure 5.4   Reactor antineutrino spectrum.

E_ν is the neutrino energy, L is the distance from reactor to the Jinping detector, θ_{12} and ΔM_{21}^2 are oscillation parameters. Where L can be calculated using the latitude and longitude between the reactors and Jinping detector. The value of $\sin\theta_{12} = 0.586$ and $\Delta M_{21}^2 = 7.58 \times 10^{-5}$ eV. The total flux at Jinping from all the current or under construction reactors as shown in Fig. 5.5.
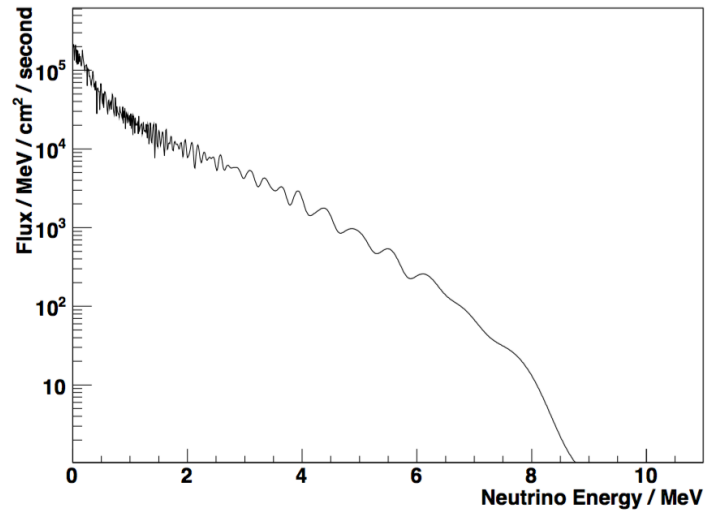
Figure 5.5   Total flux at Jinping.

5.6.1.3   Reactors in operation and under construction

There are 34 operational and 21 under construction reactor in China. The list of the operational reactors are shown in Tab. 5.8 and map is also shown in the Fig. 5.6. The

list of the under construction reactors are shown in Tab. 5.9 and map is also shown in the Fig. 5.7. We estimated the distance from each reactor to CJPL, by using the latitude and longitude.

Figure 5.6　　Map of the operational reactors in China (Google maps).

Figure 5.7　　Map of the under construction reactors in China (Google maps).

5.6.1.4　Impact of inland reactors

According to Ref.[89] many inland reactors are future planned in mainland China. Fig. 5.8 shows the possible locations of inland nuclear power plants in China. Since the reactor neutrino flux propagates according to the inverse square of distance to CJPL.

Table 5.8   List of operational reactors in China[89].
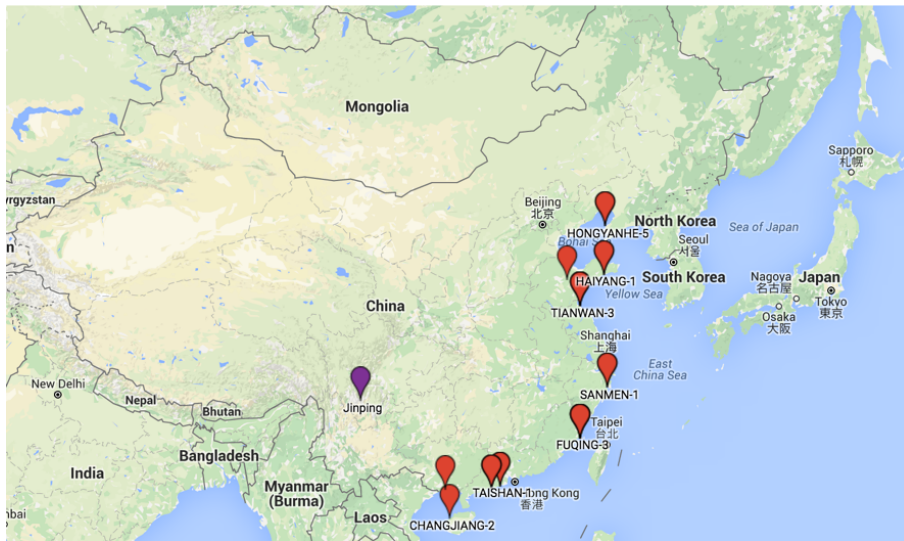
Sitename	Latitude	Longitude	Power (Gw)	Distance to CJPL (km)
CHANGJIANG-2	19.46075	108.899917	1.93	1217.4
HONGYANHE-4	39.795833	121.480556	2.905	2220.95
NINGDE-4	27.044444	120.283333	2.905	1835.02
CEFR	39.740929	116.030139	0.065	1837.94
CHANGJIANG-1	19.46075	108.899917	1.93	1217.4
DAYABAY-1	22.597222	114.544444	2.905	1434.82
DAYABAY-2	22.5953	114.5431	2.905	1434.8
FANGCHENGGANG-1	21.666667	108.566667	2.905	1006.06
FANGJIASHAN-1	30.441342	120.941758	2.905	1880.97
FANGJIASHAN-2	30.441342	120.941758	2.905	1880.97
FUQING-1	25.445833	119.447222	2.905	1787.45
FUQING-2	25.445833	119.447222	2.905	1787.45
HONGYANHE-1	39.795833	121.480556	2.905	2220.95
HONGYANHE-2	39.795833	121.480556	2.905	2220.95
HONGYANHE-3	39.795833	121.480556	2.905	2220.95
LINGAO-1	22.604789	114.551489	2.905	1435.06
LINGAO-2	22.604789	114.551489	2.905	1435.06
LINGAO-3	22.604789	114.551489	2.905	1435.06
LINGAO-4	22.604789	114.551489	2.905	1435.06
NINGDE-1	27.044444	120.283333	2.905	1835.02
NINGDE-2	27.044444	120.283333	2.905	1835.02
NINGDE-3	27.044444	120.283333	2.905	1835.02
QINSHAN2-1	30.433056	120.95	1.93	1881.7
QINSHAN2-2	30.433056	120.95	1.93	1881.7
QINSHAN2-3	30.433056	120.95	1.93	1881.7
QINSHAN2-4	30.433056	120.95	1.93	1881.7
QINSHAN3-1	30.433056	120.95	2.064	1881.7
QINSHAN3-2	30.433056	120.95	2.064	1881.7
QINSHAN1	30.433056	120.95	0.966	1881.7
TIANWAN-1	34.686944	119.459722	3	1830.88
TIANWAN-2	34.686944	119.459722	3	1830.88
YANGJIANG-1	21.708333	112.261111	2.905	1288.64
YANGJIANG-2	21.708333	112.261111	2.905	1288.64
YANGJIANG-3	21.708333	112.261111	2.905	1288.64

Table 5.9   List of under construction reactors in China[89].

Sitename	Latitude	Longitude	Power (Gw)	Distance to CJPL (km)
CHANGJIANG-2	19.46075	108.899917	1.93	1217.4
FANGCHENGGANG-2	21.666667	108.566667	2.905	1006.06
FUQING-3	25.445833	119.447222	2.905	1787.45
FUQING-4	25.445833	119.447222	2.905	1787.45
FUQING-5	25.445833	119.447222	2.905	1787.45
FUQING-6	25.445833	119.447222	2.905	1787.45
HAIYANG-1	36.708333	121.383333	3.451	2068.01
HAIYANG-2	36.708333	121.383333	3.451	2068.01
HONGYANHE-5	39.795833	121.480556	2.905	2220.95
HONGYANHE-6	39.795833	121.480556	2.905	2220.95
SANMEN-1	29.101111	121.641944	3.4	1946.62
SANMEN-2	29.101111	121.641944	3.4	1946.62
SHIDAOBAY-1	36.4	118.4	0.5	1812.85
TAISHAN-1	21.917778	112.981944	4.59	1336.18
TAISHAN-2	21.917778	112.981944	4.59	1336.18
TIANWAN-3	34.686944	119.459722	3	1830.88
TIANWAN-4	34.686944	119.459722	3	1830.88
TIANWAN-5	34.686944	119.459722	2.905	1830.88
YANGJIANG-4	21.708333	112.261111	2.905	1288.64
YANGJIANG-5	21.708333	112.261111	2.905	1288.64
YANGJIANG-6	21.708333	112.261111	2.905	1288.64

A factor of two shorter distance will cause a factor of four increase for the flux for the reactors with the same thermal power. Assuming the inland reactors with 2.9 GW thermal power each and an average distance L of ~561 km, we expect the reactor neutrino background will increase 0.0100 events/day/kiloton times.
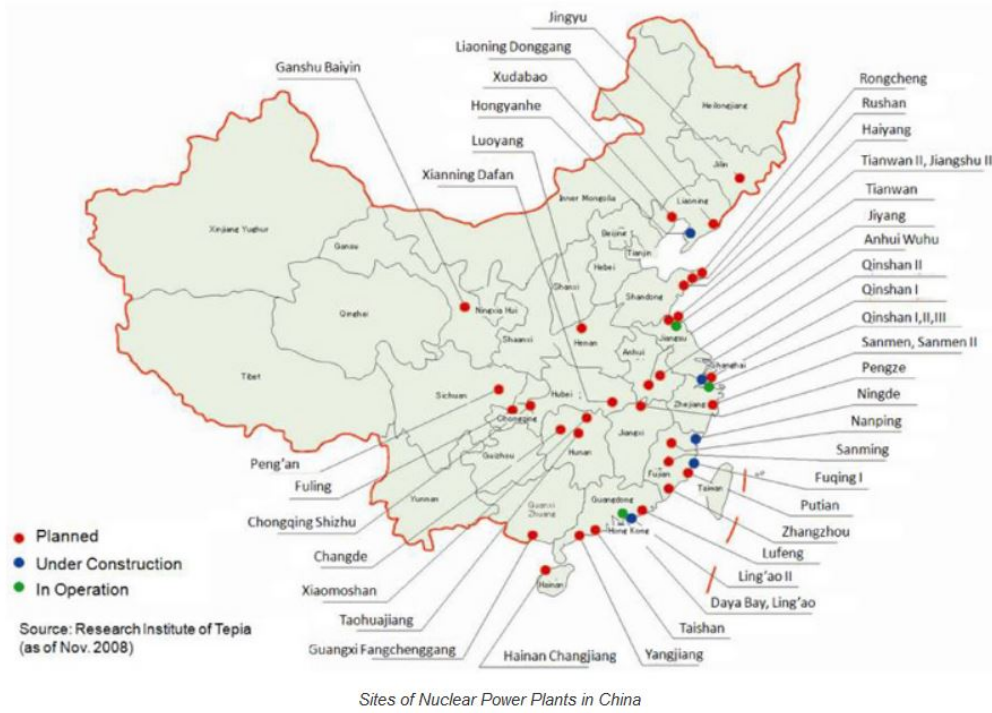

Figure 5.8   Map of inland reactors.

In Fig. 5.9, the color online, comparison of reactor neutrino flux at Jinping and other underground experiments, such as: Gran Sasso, Kamioka and others. The CJPL has lowest reactor antineutrino rate $1.3 \times 10^6/(\text{cm}^2 \cdot \text{s})$.

5.6.1.5   Total reactor neutrino event rate

Electron anti-neutrino's will be detected via IBD process,

$$\bar{\nu}_e + \text{p} \rightarrow \text{e}^+ + \text{n}. \tag{5-11}$$

The above reaction needs a threshold 1.8 MeV and what we measured, E_{vis}, is the sum of positron energy and two 0.511 MeV gammas,

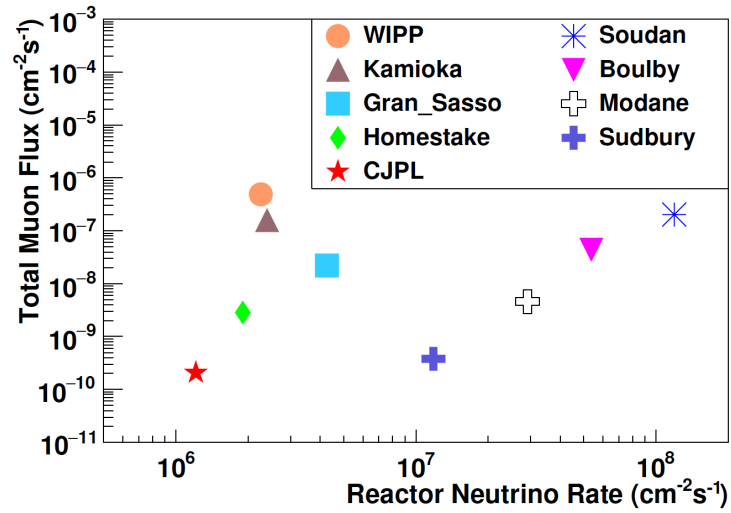$$E_{vis} = E_\nu - 0.78 \text{MeV}. \tag{5-12}$$

Figure 5.9   Total muon flux vs. reactor antineutrino flux[16].

Figure 5.10   IBD cross section.

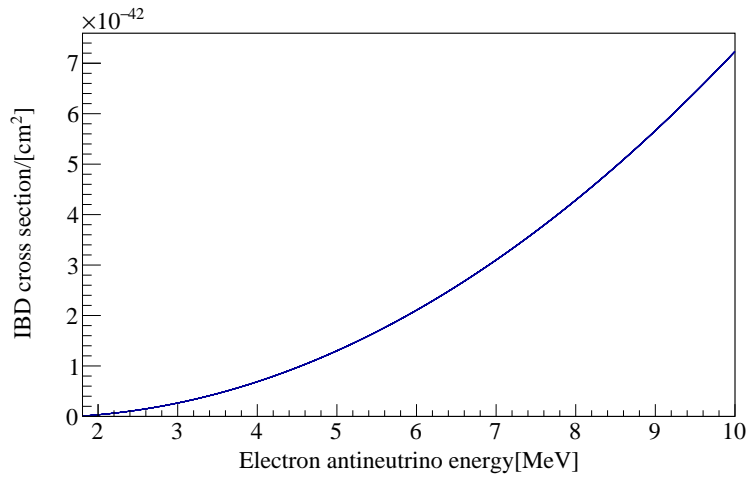By calculating the total flux from all the nuclear reactors (under construction and operational) and the cross section of IBD, $\sigma(E_v)$[16] as shown in Fig. 5.10, one can measure the rate of detectable events at Jinping using the Equation (5-13), total reactor v_e event rate as shown in Table 5.10 and also in Figure 5.11,

$$R_{Jinping}(E_v) = \phi_{Jinping}(E_v) \times \sigma(E_v). \tag{5-13}$$

Table 5.10   Reactor ν_e event rate at Jinping. 1 TNU=(1 event/10^{32}protons/year).

Event rate	Constructed		Under construction		Total
(TNU)	China	Others	China	Others	
FER (1.8-10.0 MeV)	8.9 ± 0.2	10.6 ± 0.1	6.3 ± 0.1	2.0 ± 0.0	27.8 ± 0.4
SER (1.8-3.3 MeV)	2.4 ± 0.1	2.3 ± 0.0	1.5 ± 0.0	0.6 ± 0.0	6.8 ± 0.1
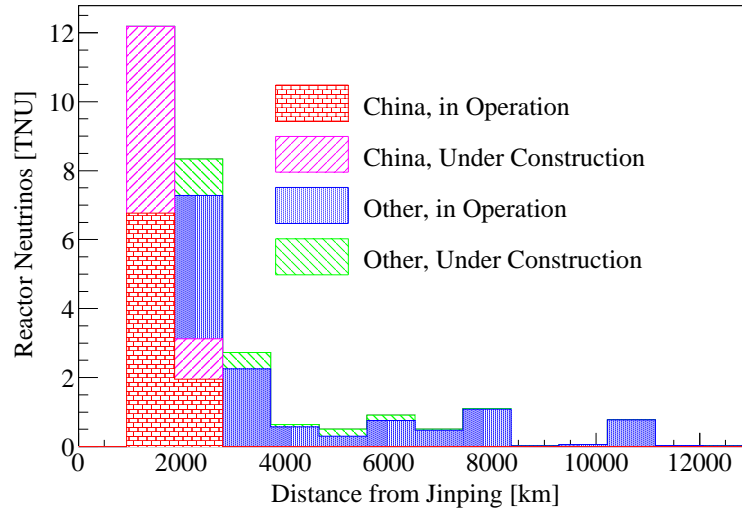
Figure 5.11   Reactor ν_e background spectra at jinping, from all reactors (operational and under construction) in China and others.

5.6.2   Non-neutrino backgrounds

Li-He: When high energy muons (μ's) go through the detector, it can have a strong interaction with the LS, mainly the carbon nuclei, producing fast neutrons and some radioisotopes. Among these isotopes, the ^{9}Li and ^{9}He nuclei can have β-neutron cascade decay. The muon flux is very low at Jinping. A μ veto cut of 2s is applied at a cost of loss in 1.1% live time. The estimated background rate of ^{9}Li and ^{9}He is $0.02 \pm 0.01/3$ kilotons $\times$ 1,500 days.

Fast neutrons: Fast neutrons backgrounds are also produced due to muons, when high energy μ's go through the detector. A μ veto cut of 2s is applied, causing a loss in 1.1% live time. The estimated background rate of fast neutron is $\leq 0.04/3$ kilotons $\times$ 1,500 days.

Alpha-neutron   There are many radioisotopes, which emit the alpha particles, they can also trigger the alpha-neutron reaction in LS. ^{210}Po background plays an important role in

measuring the background rate of (α, n) for geoneutrino measurements. By considering the identical level of ^{210}Po background such as Borexino[27], the estimated background rate of alpha-neutron is $(1.7 \pm 0.1)/3$ kilotons/1,500 days. Accidental backgrounds are ignored, considering the cleanness of detector and use the fiducial volume cut to veto the outside natural radioactivity[16].

The summary of all the non neutrino background is shown in Table 5.11,

Table 5.11   Total non antineutrino backgrounds events with an exposure of 3 kilotons $\times$ 1,500 days at Jinping.

	^{9}Li $-^8$ He	Fast neutrons	$\alpha - $n	Total
		3 kilotons $\times$ 1,500 days		
Events	0.02 ± 0.01	≤ 0.04	1.7 ± 0.1	1.8

The total non-neutrino background is 1.8/3 kilotons/1,500 days as shown in Table 5.11 and is ignored in this thesis, as comparing to reactor ν_e background rate is $(60.4 \pm 0.9)/3$ kilotons/1,500 days, as shown in Table 5.13.

5.7   IBD spectrum at Jinping

By considering the 500 p.e./MeV with energy resolution $(4.4\%/\sqrt{E_{vis}})$, the target mass of 3 kilotons and with live time of 1,500 days, expected IBD spectra as shown in Fig. 5.12. Geoneutrinos predictions for Jinping are categorized in Table 5.12. Geoneutrino signal and reactor $\bar{\nu}_e$'s background, event rates are enlisted in Table 5.13.

Table 5.12   Summary of predicted geoneutrino event rates in TNU at Jinping.

Geo $\bar{\nu}_e$ (TNU)	Crust	Mantle	BSE
Th	10.6 ± 0.8	2.1 ± 0.5	12.7 ± 1.0
U	38.4 ± 6.6	8.3 ± 2.3	46.7 ± 6.7
Th+U	49.0 ± 7.3	10.4 ± 2.7	59.4 ± 7.6

5.8   Summary

In this chapter, we estimated the geoneutrino signal for ^{238}U $= 46.7 \pm 6.7$ and ^{232}Th $= 12.7 \pm 1.0$ TNU and for the reactor background in signal region (1.8-3.3 MeV) is 6.8 $\pm$
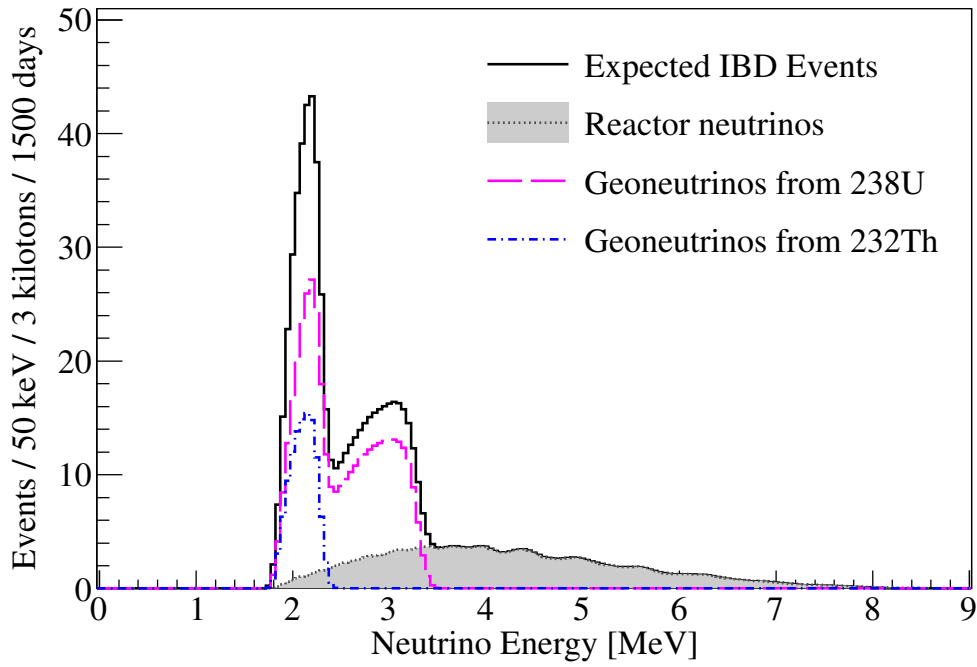
Figure 5.12   Jinping expected IBD spectrum, black solid line represents the total number of events, blue and magenta dashed lines indicates the geoneutrinos from ^{232}Th and ^{238}U , respectively. Grey filled is the reactor $\bar{\nu}_e$'s.

Table 5.13   Geoneutrino and reactor neutrino event rates and total events with an exposure of 3 kilotons × 1,500 days at Jinping.

	Geoneutrino			Reactor	
	^{238}U	^{232}Th	Total	FER	SER
Event Rate (TNU)	46.7	12.7	59.4	27.8	6.8
Total Events	414.5	113.6	527.3	246.8	60.4

0.1, and in full region (1.8-10.0 MeV) is 27.8±0.4 TNU, respectively. Non-neutrino backgrounds have been ignored in this study.

Chapter 6   Conclusion

Neutrinos have been a common interest among the study of particle physics, nuclear physics, astrophysics and cosmology, and hence have important scientific significance and great potential application. The proposed low-energy neutrino experiment at China JinPing underground Lab (CJPL) with the largest overburden in the world, has natural advantages of lowest cosmic background and reactor neutrino background, as well as the highest geoneutrino flux, specifically suitable for relevant physics studies on solar neutrinos and geoneutrinos. This thesis has focused on the issues and applications of the radioactive nucleus decays for the solar and geoneutrino experiment at Jinping. The summaries are as follows:

1) We investigated the whole smelting procedure to produce the low level background SST. We adopted different assay methods to investigate the contaminations in our samples. We used professional facilities like GDMS to measure the radioactivity in our samples.

A low background HPGe(CJPL) facility, was installed at CJPL and used for various detector's material testing, including to investigate materials for Jinping neutrino experiment, which is very sensitive to the rare event and also for the environmental monitoring. We have reported our comparison with other experiments with respect to the radioactivity in SST.

2) We estimated the geoneutrino signal for ^{238}U = 46.7 ± 6.7 and ^{232}Th = 12.7 ± 1.0 TNU and for the reactor background in signal region (1.8-3.3 MeV) is 6.8 ± 0.1, and in full region (1.8-10.0 MeV) is 27.8 ± 0.4 TNU, respectively. Non-neutrino backgrounds has been ignored in this study.

Reference

[1]   W. Pauli, *Dear radioactive ladies and gentlemen*, Phys. Today31N9 (1978) 27.

[2]   C. L. Cowan *et al.*, *Detection of the free neutrino: A Confirmation*, Science124 (1956) 103.

[3]   G. Danby *et al.*, *Observation of High-Energy Neutrino Reactions and the Existence of Two Kinds of Neutrinos*, Phys. Rev. Lett. 9 (1962) 36.

[4]   DONUT, K. Kodama *et al.*, *Observation of tau neutrino interactions*, Phys. Lett. B504 (2001) 218, `arXiv:hep-ex/0012035`.

[5]   B. Pontecorvo, *Neutrino Experiments and the Problem of Conservation of Leptonic Charge*, Sov. Phys. JETP26 (1968) 984.

[6]   Particle Data Group, K. A. Olive *et al.*, *Review of Particle Physics*, Chin. Phys. C38 (2014) 090001.

[7]   C. Giunti and C. W. Kim, *Fundamentals of Neutrino Physics and Astrophysics*, 2007.

[8]   H. Bei-Zhen, *The measurement of mixing angle θ_{13} from delayed neutron capture on hydrogen in the Daya Bay reactor neutrino experiment*, PhD thesis, NCTU, 2014.

[9]   P. Lipari, *Neutrinos, a different way to look at the sky*, Acta Phys. Polon. B37 (2006) 2411.

[10]   Daya Bay, F. P. An *et al.*, *Measurement of the Reactor Antineutrino Flux and Spectrum at Daya Bay*, `arXiv:1508.0423`.

[11]   RENO, J. H. Choi *et al.*, *Observation of Energy and Baseline Dependent Reactor Antineutrino Disappearance in the RENO Experiment*, `arXiv:1511.0584`.

[12]   *Solar neutrinos: The first thirty years: Edited by john n. bahcall, raymond davis, jr., peter parker, alexei smirnov, and roger ulrich. westview press, boulder, co. (2002). 462 pages. 50*, Computers and Mathematics with Applications46 (2003), no. 2–3 513 .

[13]   *http://cds.cern.ch/record/545258/files/0203272.pdf*, .

[14]   Particle Data Group, C. Amsler *et al.*, *Review of Particle Physics*, Phys. Lett. B667 (2008) 1.

[15]   MINOS, D. G. Michael *et al.*, *Observation of muon neutrino disappearance with the MINOS detectors and the NuMI neutrino beam*, Phys. Rev. Lett. 97 (2006) 191801, `arXiv:hep-ex/0607088`.

[16]   J. F. Beacom *et al.*, *Letter of Intent: Jinping Neutrino Experiment*, Chin. Phys. C41 (2017), no. 2 023002, `arXiv:1602.0173`.

[17]   R. Davis, Jr., D. S. Harmer, and K. C. Hoffman, *Search for neutrinos from the sun*, Phys. Rev. Lett. 20 (1968) 1205.

[18]   SAGE, J. N. Abdurashitov *et al.*, *Measurement of the solar neutrino capture rate by SAGE and implications for neutrino oscillations in vacuum*, Phys. Rev. Lett. 83 (1999) 4686, `arXiv:astro-ph/9907131`.

[19]   GNO, M. Altmann *et al.*, *Complete results for five years of GNO solar neutrino observations*, Phys. Lett. B616 (2005) 174, `arXiv:hep-ex/0504037`.

[20] Kamiokande, Y. Fukuda *et al.*, *Solar neutrino data covering solar cycle 22*, Phys. Rev. Lett. 77 (1996) 1683.

[21] SNO, B. Aharmim *et al.*, *Electron energy spectra, fluxes, and day-night asymmetries of B-8 solar neutrinos from measurements with NaCl dissolved in the heavy-water detector at the Sudbury Neutrino Observatory*, Phys. Rev. C72 (2005) 055502, `arXiv:nucl-ex/0502021`.

[22] Borexino, C. Arpesella *et al.*, *Direct Measurement of the Be-7 Solar Neutrino Flux with 192 Days of Borexino Data*, Phys. Rev. Lett. 101 (2008) 091302, `arXiv:0805.3843`.

[23] Super-Kamiokande, J. Hosaka *et al.*, *Solar neutrino measurements in super-Kamiokande-I*, Phys. Rev. D73 (2006) 112001, `arXiv:hep-ex/0508053`.

[24] G. Eder, *Terrestrial neutrinos*, Nuclear Physics A78 (1966) 657.

[25] L. M. Krauss *et al.*, *Anti-neutrinos Astronomy and Geophysics*, Nature310 (1984) 191.

[26] T. Araki *et al.*, *Experimental investigation of geologically produced antineutrinos with kamland*, Nature436 (2005) 499.

[27] Borexino, G. Bellini *et al.*, *Observation of Geo-Neutrinos*, Phys. Lett. B687 (2010) 299, `arXiv:1003.0284`.

[28] W. McDonough and O. Šrámek, *Neutrino geoscience, news in brief*, Environmental Earth Sciences71 (2014), no. 8 3787.

[29] *Partial radiogenic heat model for earth revealed by geoneutrino measurements*, Nature Geosci4 (2011) 647.

[30] KamLAND, A. Gando *et al.*, *Reactor On-Off Antineutrino Measurement with KamLAND*, Phys. Rev. D88 (2013), no. 3 033001, `arXiv:1303.4667`.

[31] Borexino, G. Bellini *et al.*, *Measurement of geo-neutrinos from 1353 days of Borexino*, Phys. Lett. B722 (2013) 295, `arXiv:1303.2571`.

[32] Borexino, M. Agostini *et al.*, *Spectroscopy of geoneutrinos from 2056 days of Borexino data*, Phys. Rev. D92 (2015), no. 3 031101, `arXiv:1506.0461`.

[33] JUNO, Z. Djurcic *et al.*, *JUNO Conceptual Design Report*, `arXiv:1508.0716`.

[34] SNO+, S. Andringa *et al.*, *Current Status and Future Prospects of the SNO+ Experiment*, Adv. High Energy Phys. 2016 (2016) 6194250, `arXiv:1508.0575`.

[35] LENA, M. Wurm *et al.*, *The next-generation liquid-scintillator neutrino observatory LENA*, Astropart. Phys. 35 (2012) 685, `arXiv:1104.5620`.

[36] N. Tolich *et al.*, *A Geoneutrino experiment at Homestake*, `arXiv:physics/0607230`, [Earth Moon Planets99,229(2006)].

[37] I. R. Barabanov, G. Ya. Novikova, V. V. Sinev, and E. A. Yanovich, *Research of the natural neutrino fluxes by use of large volume scintillation detector at Baksan*, 1228-2009`arXiv:0908.1466`.

[38] *http://www.geoneutrino.nl/*, .

[39] J. G. Learned, S. T. Dye, and S. Pakvasa, *Hanohano: A Deep ocean anti-neutrino detector for unique neutrino physics and geophysics studies*, in *Neutrino telescopes. Proceedings, 12th International Workshop, Venice, Italy, March 6-9, 2007*, pp. 235–269, 2007. `arXiv:0810.4975`.

Reference

[40] C. Arpesella *et al.*, *Measurements of extremely low radioactivity levels in {BOREXINO}*, Astroparticle Physics18 (2002), no. 1 1 .

[41] CDEX, K. Kang *et al.*, *Introduction to the CDEX experiment*, Front. Phys. (Beijing)8 (2013) 412, `arXiv:1303.0601`.

[42] *Measurements of extremely low radioactivity levels in stainless steel for {GERDA}*, Nuclear Instruments and Methods in Physics Research Section A: Accelerators, Spectrometers, Detectors and Associated Equipment593 (2008), no. 3 448 .

[43] S. Kai, *Alpha-, Beta- and Gamma-Ray Spectroscopy*, Elsevier, 1968.

[44] A. Fay, *Nuclear Spectroscopy*, Elsevier, 1960.

[45] G. Li, *Estimation of solar neutirno radioactive background*, PhD thesis, Tsighua University, 2014.

[46] L. Durand, *Electron screening corrections to beta-decay spectra*, Phys. Rev. 135 (1964) B310.

[47] D. Wilkinson, *Evaluation of beta-decay*, Nuclear Instruments and Methods in Physics Research Section A290 (1990), no. 2 509 .

[48] P. Huber, *On the determination of anti-neutrino spectra from nuclear reactors*, Phys. Rev. C84 (2011) 024617, `arXiv:1106.0687`.

[49] G. Fiorentini *et al.*, *Nuclear physics for geo-neutrino studies*, Phys. Rev. C81 (2010) 034602, `arXiv:0908.3433`.

[50] K. J. Kang, *et al.*, *Status and prospects of a deep underground laboratory in china*, Journal of Physics: Conference Series203 (2010), no. 1 012028.

[51] F. Duncan *et al.*, *The Construction and Anticipated Science of SNOLAB*, Annual Review of Nuclear and Particle Science60 (2010), no. 1 163.

[52] C. Arpesella, *A low background counting facility at laboratori nazionali del gran sasso*, Applied Radiation and Isotopes47 (1996), no. 9 991 .

[53] C. Zhang, *Precision measurement of neutrino oscillation parameters and investigation of nuclear georeactor hypothesis with KamLAND*, PhD thesis, Caltech, 2010.

[54] Y. C. Wu *et al.*, *Measurement of Cosmic Ray Flux in China JinPing underground Laboratory*, Chin. Phys. C37 (2013), no. 8 086001, `arXiv:1305.0899`.

[55] M. Li *et al.*, *Separation of Scintillation and Cherenkov Lights in Linear Alkyl Benzene*, Nucl. Instrum. Meth. A830 (2016) 303, `arXiv:1511.0933`.

[56] *Design and analysis of a 1-ton prototype of the jinping neutrino experiment*, Nuclear Instruments and Methods in Physics Research Section A: Accelerators, Spectrometers, Detectors and Associated Equipment855 (2017) 81 .

[57] T. Zhang *et al.*, *Low Background Stainless Steel for the Pressure Vessel in the PandaX-II Dark Matter Experiment*, JINST11 (2016), no. 09 T09004, `arXiv:1609.0751`.

[58] M. Hult, *Low-level gamma-ray spectrometry using ge-detectors*, Metrologia44 (2007), no. 4 S87.

[59] L. Baudis *et al.*, *Gator: a low-background counting facility at the Gran Sasso Underground Laboratory*, JINST6 (2011) P08010, `arXiv:1103.2125`.

[60] D. Budjas *et al.*, *Gamma-ray spectrometry of ultra low levels of radioactivity within the material screening program for the GERDA experiment*, Appl. Radiat. Isot67 (2009) 755–758.

[61] G. Heusser, *Low-radioactivity background techniques*, Ann. Rev. Nucl. Part. Sci. 45 (1995) 543.

[62] M. Hult *et al.*, *Underground gamma-ray spectrometry*, Acta Chim. Slov. 53 (2006) 1.

[63] M. Laubenstein *et al.*, *Underground measurements of radioactivity*, Applied Radiation and Isotopes61 (2004), no. 2šC3 167 , Low Level Radionuclide Measurement Techniques - {ICRM}.

[64] M. Kohler *et al.*, *A new low-level γ-ray spectrometry system for environmental radioactivity at the underground laboratory felsenkeller*, Applied Radiation and Isotopes67 (2009), no. 5 736 , 5th International Conference on Radionuclide Metrology - Low-Level Radioactivity Measurement Techniques ICRM-LLRMT'08.

[65] A. Zastawny, *The Measurements of low radioactivities*.

[66] M. Betti *et al.*, *Detection of trace radioisotopes in soil, sediment and vegetation by glow discharge mass spectrometry*, Fresenius' Journal of Analytical Chemistry355 (1996), no. 5 642.

[67] M. Betti, *Isotope ratio measurements by secondary ion mass spectrometry (SIMS) and glow discharge mass spectrometry (GDMS)* , International Journal of Mass Spectrometry242 (2005), no. 2SC3 169 , Isotope Ratio Measurements {SI}.

[68] L. Aldave de las Heras, E. Hrnecek, O. Bildstein, and M. Betti, *Neptunium determination by dc glow discharge mass spectrometry (dc-gdms) in irish sea sediment samples*, J. Anal. At. Spectrom. 17 (2002) 1011.

[69] M. Betti, *Use of a direct current glow discharge mass spectrometer for the chemical characterization of samples of nuclear concern*, J. Anal. At. Spectrom. 11 (1996) 855.

[70] Z. Zhi *et al.*, *Geant4 applications in nuclear technology*, Journal of Isotopes (2004).

[71] Y. Mi *et al.*, *The characteristics of a low background germanium gamma ray spectrometer at China JinPing underground Laboratory*, `arXiv:1403.1724`.

[72] X. Wang *et al.*, *Material Screening with HPGe Counting Station for PandaX Experiment*, JINST11 (2016), no. 12 T12002, `arXiv:1608.0834`.

[73] G. R. Gilmore, *Practical Gamma-Ray Spectrometry*, John Wiley & Sons, Ltd, 2008.

[74] S. Cebrián *et al.*, *Radon and material radiopurity assessment for the NEXT double beta decay experiment*, AIP Conf. Proc. 1672 (2015) 060002, `arXiv:1505.0705`.

[75] H. N. Pollack *et al.*, *Heat flow from the earth's interior: Analysis of the global data set*, Reviews of Geophysics31 (1993), no. 3 267.

[76] A. Hofmeister and R. Criss, *Earth's heat flux revised and linked to chemistry*, Tectonophysics395 (2005), no. 3–4 159 .

[77] W. Moon, *Mantle convection in the earth and planets by gerald schubert, donald l. turcotte and peter olson*, Geosciences Journal6 (2002), no. 3 253.

Reference

[78] R. Kippenhahn and A. Weigert, *Stellar structure and evolution*, Springer-Verlag, Berlin; New York, 1990.

[79] E. J. Chaisson, *Solar system modeling*, Tufts University (2005).

[80] C. Frankel, *Volcanoes of the Solar System*, no. ISBN 0521477700, Cambridge University Press, 1996.

[81] J. Korenaga, *A method to estimate the composition of the bulk silicate earth in the presence of a hidden geochemical reservoir*, Geochimica et Cosmochimica Acta73 (2009), no. 22 6952 .

[82] W. McDonough and S. s. Sun, *The composition of the earth*, Chemical Geology120 (1995), no. 3–4 223 , Chemical Evolution of the Mantle.

[83] S. Enomoto, E. Ohtani, K. Inoue, and A. Suzuki, *Neutrino geophysics with kamland and future prospects*, Earth and Planetary Science Letters258 (2007), no. 1–2 147 .

[84] S. R. Taylor and S. M. McLennan, *The geochemical evolution of the continental crust*, Reviews of Geophysics33 (1995), no. 2 241.

[85] T. Plank and C. H. Langmuir, *The chemical composition of subducting sediment and its consequences for the crust and mantle*, Chemical Geology145 (1998), no. 3–4 325 .

[86] Y. Huang and others", *A reference earth model for the heat-producing elements and associated geoneutrino flux*, Geochemistry, Geophysics, Geosystems14 (2013), no. 6 2003.

[87] L. Ludhova and S. Zavatarelli, *Studying the Earth with Geoneutrinos*, `arXiv:1310.3961`.

[88] S. Enomoto, *Neutrino geophysics and observation of geoneutrinos at KamLAND*, PhD thesis, Tohoku University, 2005.

[89] *International atomic agency*, .

Acknowledgement

First of all, I would like to thank you Prof. **Chen Shaomin**, who made my dream comes true. He gave me an opportunity to learn the physics in a new way, who really showed me what high energy and neutrino physics is. He holds my hand like a child and show me the right track to do research. I have no worlds to say thanks to him. He taught me many subjects during my tenure in Tsinghua University. He is not only teacher but also a best friend to me. Whenever, I have any issue, he is ready to help me. He solve my many issues in these years. He is very kind and look after me like his own kid. This work can not reach at that level, without of his guidance and affection.

A very special thanks goes to Prof. Wang Zhe, who helped me in every matter of life. He guides me step by step to reach today's level of research. He is also very friendly and great teacher.

I am also thankful to Prof. Gao Yuaning and Prof. Zhu Xianglei, for teaching me Particle physics. They are also nicest teachers, I ever met. I am also thankful to Prof. Yang Zhenwei, who introduced ROOT, Geant4, and Linux to me. I am also thankful to Prof. Zeng Zhi, who helps me to understand this work.

I should say thanks to my all fellows, from the previous years to present including Zhang Yiming, Fan Jingzhou, Wan Linyan, Wang Xiongfei, Zhong Liang, Xia Ligang, Li Gang, Li Bo, Wei Hanyu, Ji Xiangpan, Zhang Yang, Jia Yin, M. Usman Ashraf and others. They guide me in my research and other useful matters. I am also thankful to Dr. Adam Davis for his suggestions and proof reading of this thesis.

I should be very grateful to my parents who helped me to pay my fees during my study at Tsinghua. I believe it's not possible with out there support.

Finally, I would like say thanks to my wife and my daughter(Aswah), they accompany me all the time.

声　明

本人郑重声明：所呈交的学位论文，是本人在导师指导下，独立进行研究工作所取得的成果。尽我所知，除文中已经注明引用的内容外，本学位论文的研究成果不包含任何他人享有著作权的内容。对本论文所涉及的研究工作做出贡献的其他个人和集体，均已在文中以明确方式标明。

签　名：_____　日　期：_____

Resume and publications

Resume

- Feb. 1983, born in Lahore, Islamic Republic of Pakistan
- Sep. 2003 - Jan. 2007, B.Sc in Physics.
  Punjab University, Lahore, Islamic Republic of Pakistan
- Sep. 2007 - Jan. 2010, M.Sc in Medical Physics.
  Department of Physics, The Islamia University of Bahawalpur, Punjab, Islamic Republic of Pakistan
- Sep. 2011 - present, Ph.D. candidate in Engendering Physics.
  Department of Engineering Physics, Tsinghua University, Beijing, China

Publications

[1] Wan, Linyan and Ghulam Hussain, Geoneutrinos at Jinping: Flux prediction and oscillation analysis, Phys. Rev. D**95**, 053001 (2017). arXiv:1612.00133.

[2] F. P. An, *et al.* (Daya Bay Collaboration), *Independent measurement of the neutrino mixing angle θ_{13} via neutron capture on hydrogen at Daya Bay*, Phys. Rev. D **90**, 071101(R) (2014). arXiv:1406.6468.

[3] Ghulam Hussain *et al.*, A study of low background stainless steel for the neutrino experiment at Jinping [submit soon].